Pacific Northwest
NATIONAL LABORATORY

PNNL-38112

Laser Powder Directed Energy Deposition of Steels for Nuclear Applications

M3MT-25PN0902031

August 2025

Subhashish Meher
Asif Mahmud
Isabella J van Rooyen

U.S. DEPARTMENT of ENERGY

Prepared for the U.S. Department of Energy
under Contract DE-AC05-76RL01830

DISCLAIMER

PACIFIC NORTHWEST NATIONAL LABORATORY
operated by
BATTELLE
for the
UNITED STATES DEPARTMENT OF ENERGY
under Contract DE-AC05-76RL01830

Printed in the United States of America

Available to DOE and DOE contractors from
the Office of Scientific and Technical Information,
P.O. Box 62, Oak Ridge, TN 37831-0062
www.osti.gov
ph: (865) 576-8401
fox: (865) 576-5728
email: reports@osti.gov

Available to the public from the National Technical Information Service
5301 Shawnee Rd., Alexandria, VA 22312
ph: (800) 553-NTIS (6847)
or (703) 605-6000
email: info@ntis.gov
Online ordering: http://www.ntis.gov

PNNL-38112

Laser Powder Directed Energy Deposition of Steels for Nuclear Applications

M3MT-25PN0902031

August 2025

Subhashish Meher
Asif Mahmud
Isabella J van Rooyen

Prepared for
the U.S. Department of Energy
under Contract DE-AC05-76RL01830

Pacific Northwest National Laboratory
Richland, Washington 99354

Abstract

This comprehensive investigation examines the structure–property relationships in two nuclear alloy systems—Alloy 709 (A709) austenitic stainless steel and Grade 92 (G-92) ferritic/martensitic (F/M) steel—manufactured via directed energy deposition (DED) for sodium-cooled fast reactor applications. This study establishes the fundamental mechanisms for controlling microstructures for optimizing the mechanical performance of additively manufactured nuclear materials through systematic heat treatment optimization and multiscale characterization.

As-deposited A709 steel develops a complex multiscale strengthening architecture consisting of a fine cellular solidification structure with diameter of 2-3 μm within10–50 μm grains, elevated dislocation densities from rapid thermal cycling, and grain boundary precipitates that activate concurrent Hall–Petch, dislocation, and precipitation hardening mechanisms to achieve exceptional properties [yield strength (YS): 603 MPa, ultimate tensile strength (UTS): 844 MPa, Vickers hardness: 220 HV] that achieve a 44% superior strength compared to that of the wrought material. Heat treatments produce different results. Solution annealing (SA) dissolves the cellular structure and reduces the hardness to 190 HV. Precipitation treatment (PT) keeps the cellular structure but adds carbides, allowing the hardness to reach 205 HV. The best approach combines both treatments (SA+PT) and creates uniform precipitate distributions with $M_{23}C_6$ carbides at the grain boundaries and MX carbonitrides in the matrix, achieving a hardness of 195 HV. However, directional differences persist, with a 12%–15% strength variation between orientations due to the inherited layered microstructural architecture that survives aggressive heat treatment. While tensile testing at 550°C demonstrates 40%–50% thermal softening with dynamic strain aging, DED A709 steel still maintains a 71% higher YS than that of the wrought material. Ion irradiation studies (100–400 dpa) of DED A709 steel reveal progressive radiation damage with increasing void density and radiation-induced segregation causing nickel enrichment and chromium depletion, which will ultimately compromise mechanical properties.

As-deposited G-92 exhibits exceptional strength (UTS: 1650–1700 MPa, 430 HV) through a complex microstructure containing both ferrite and martensite phases, a high geometrically necessary dislocation (GND) density ($17.04\times10^{14}/m^2$), and fine carbides. Heat treatments create distinct changes. Normalizing produces fresh martensite with the highest hardness (460 HV) and an increased GND density ($20.23\times10^{14}/m^2$). Tempering develops dual precipitation systems and reduces the hardness to 290 HV. The optimal approach uses sequential normalizing plus tempering, achieving balanced properties with the lowest hardness (250 HV) and a reduced GND density ($11.01\times10^{14}/m^2$). A processing-dependent anisotropy is observed: horizontal specimens achieve superior ductile behavior, while vertical specimens exhibit brittle failure. A tempering heat treatment successfully mitigates this anisotropic behavior by transforming the hard martensitic as-deposited structure into tempered martensite enabling both horizontal and vertical specimens to exhibit similar stress–strain characteristics with visible necking behavior. Remarkably, testing at 550°C reveals a reversal in the anisotropy, while as-deposited specimens achieve near isotropy with superior thermal stability (a 15%–20% strength reduction), while tempered specimens develop an orientation dependence with a 25%–30% strength reduction.

Both alloy systems demonstrate that DED processing creates specimens with a superior strength through refined microstructural features, though with distinct strengthening mechanisms—austenitic through cellular structures and precipitates versus F/M through phase

transformations and precipitates. Heat treatment optimization requires alloy-specific approaches, with A709 benefiting from controlled precipitation while G-92 requires careful phase transformation control. The results show that DED manufacturing can produce nuclear materials with exceptional performance, but directional effects and temperature-dependent behavior must be carefully considered for reactor component design and qualification.

Acknowledgments

The research presented herein was supported by the Advanced Materials and Manufacturing Technology (AMMT) program of the U.S. Department of Energy (DOE), Office of Nuclear Energy. Pacific Northwest National Laboratory (PNNL) is a multiprogram national laboratory operated for the DOE by Battelle Memorial Institute under Contract No. DE-AC05-76RL01830. We would like to acknowledge Prof. Xiaoyuan Lou and students John Snitzer and Qianwen Zhang from Purdue University for the laser directed energy deposition of Alloy 709 and Grade-92 steels on behalf of PNNL. We would also like to acknowledge the contributions of the following PNNL staff: Dave Olson (extracting tensile specimens from fabricated blocks), Mark Rhodes (assistance with the heat treatments), Alan L Schemer-Kohrn (assistance with electron backscatter diffraction [EBSD]), Rob Seffens and Jorge Ortiz (conducting tensile testing), and the entire metallography team at 3410 (sample preparation).

In addition to the planned scope of the work, the authors gratefully acknowledge the support provided by the Nuclear Science User Facilities (NSUF) Rapid Turnaround Experiment (RTE) program for ion irradiation of Alloy 709 reported in Section 5.0. This work was performed in support of the AMMT program's ongoing investigation efforts to evaluate advanced materials fabrication techniques. The NSUF-RTE facility access and technical support were instrumental in enabling the experimental characterization and analysis presented in this study.

Acronyms and Abbreviations

A709	Alloy 709
AD	as-deposited
AM	additive manufacturing
AMMT	Advanced Materials and Manufacturing Technology
ANL	Argonne National Laboratory
AR	as-received
ART	Advanced Reactor Technology
ATS	Applied Test Systems
BF	bright-field
C	carbon
Cr	chromium
DED	directed energy deposition
DOE	U.S. Department of Energy
dpa	displacement per atom
EBSD	electron backscatter diffraction
EDM	electrical discharge machining
F/M	ferritic/martensitic
FESEM	field emission scanning electron microscope
FIB	focused ion beam
FY	fiscal year
G-91	Grade 91
G-92	Grade 92
GND	geometrically necessary dislocation
HAADF	high-angle annular dark-field
HAGB	high-angle grain boundary
HR	high-resolution
IPF	inverse pole figure
KAM	kernel average misorientation
LAGB	low-angle grain boundary
LP-DED	laser powder directed energy deposition
Mn	manganese
Mo	molybdenum
N	nitrogen
Nb	niobium
NE	Office of Nuclear Energy
Ni	nickel

NSUF	Nuclear Science User Facilities
PNNL	Pacific Northwest National Laboratory
PT	precipitation treatment
RT	room temperature
RTE	Rapid Turnaround Experiment
SA	solution annealing
SEM	Scanning Electron Microscope
SFR	sodium-cooled fast reactor
SRIM	Stopping and Range of Ions in Matter
STEM	scanning tunneling electron microscope
TEM	transmission electron microscopy
Ti	titanium
UTS	ultimate tensile strength
W	tungsten
XEDS	energy-dispersive X-ray spectroscopy
YS	yield strength

Contents

Figures

Tables

1.0 Introduction

The U.S. Department of Energy (DOE), Office of Nuclear Energy (NE) has established the Advanced Materials and Manufacturing Technologies (AMMT) program as a strategic research initiative to accelerate high-performance materials development for extreme service conditions while enhancing the thermal efficiency and operational longevity of advanced nuclear reactor systems. This research framework addresses critical technological gaps in next-generation nuclear energy infrastructure by focusing on materials that can withstand elevated temperatures, corrosive media, and high-fluence neutron irradiation environments.

Through the DOE-NE Advanced Reactor Technology (ART) down-selection process in prior years, Alloy 709 (A709) has been designated for sodium-cooled fast reactor (SFR) applications because of its superior high-temperature performance compared to that of conventional 316H stainless steel (Wang et al. 2022). Additive manufacturing (AM) enables complex geometries that are impossible to fabricate using conventional methods, allowing optimized heat exchanger designs and integrated cooling channels that enhance reactor efficiency while reducing component count. AM also produces enhanced material properties through rapid solidification, eliminates welding joints that create potential failure points, and provides on-demand manufacturing capabilities that reduce supply chain dependencies and enable faster component development for nuclear applications. However, substantial knowledge gaps exist regarding the effects of the AM parameters on the microstructure and mechanical properties.

Grade 92 (G-92) steel represents a third-generation creep-resistant ferritic/martensitic (F/M) steel with tungsten and boron additions that enhance performance beyond that of Grade 91 (G-91) steel. Despite the potential for superior creep resistance at temperatures exceeding 600°C, G92 remains unqualified under nuclear codes with much less documented AM research.

In fiscal year (FY) 2024, the AMMT program completed Phase I optimization studies for the directed energy deposition (DED) processing parameters, establishing manufacturing protocols for high-density components. These investigations defined critical process windows encompassing the laser power, scan velocity, powder mass flow rates, and layer deposition thickness for both alloy systems.

The current FY 2025 research program comprises two complementary tasks to understand these materials in their AM-processed condition.

- Task 1 optimizes post-processing heat treatment protocols to achieve controlled nanoscale precipitation and understand microstructural evolution at elevated temperatures. This involves a systematic investigation of the normalizing and tempering parameters, precipitation kinetics, and phase stability. Research includes detailed microstructural characterization using advanced electron microscopy to establish relationships between the processing parameters, microstructure, and properties. With additional support from Nuclear Science User Facilities (NSUF) Rapid Turnaround Experiment (RTE) funding, preliminary irradiation studies on as-deposited (AD) DED A709 systematically evaluated the dose-dependent microstructural changes in the AM material.
- Task 2 encompasses a comprehensive mechanical property evaluation through hardness testing, room and elevated temperature tensile testing, and fractographic analysis. This task establishes property–processing relationships and validates that additively manufactured materials meet the performance requirements of wrought counterparts. Testing includes

evaluations of the yield strength (YS), ultimate tensile strength (UTS), ductility, and fracture behavior at room temperature (RT) and 550°C.

Concurrent laser powder bed fusion research at Argonne National Laboratory (ANL) provides a comparative framework for evaluating process advantages. This Pacific Northwest National Laboratory (PNNL)–ANL effort represents an advancement toward flexible, cost-effective manufacturing methodologies for next-generation nuclear applications, addressing technology gaps while establishing the foundations for advanced reactor deployment.

2.0 Materials

2.1 A709 Austenitic Steel

Austenitic stainless steels serve as the primary materials for critical nuclear components because of their favorable corrosion resistance and mechanical properties (Li et al. 2021). However, next-generation SFRs operate at significantly higher temperatures (500–700°C versus 280–320°C for light water reactors), necessitating advanced austenitic alloys with enhanced high-temperature performance.

A709 austenitic stainless steel represents a significant advancement in nuclear-grade materials, featuring an optimized composition including an elevated nitrogen (N) content (0.14–0.20 wt%), controlled titanium additions (0.20–0.40 wt%), and precise chromium (Cr; 19–22 wt%) and nickel (Ni; 24–26 wt%) contents (Zhao et al. 2020). The superior performance is derived from nitrogen, which provides solid-solution strengthening; titanium (Ti), which promotes fine TiN precipitates that enhance creep resistance; and an optimized Cr–Ni content that ensures exceptional liquid sodium corrosion resistance.

A709 has emerged as a leading SFR component candidate because of its exceptional performance at high temperature and during liquid sodium exposure and neutron irradiation (Alomari et al. 2018; Ding et al. 2019). The material demonstrates creep rupture strengths that are approximately 50% higher than that of conventional SS316 at temperatures exceeding 600°C for 100,000-hour service lives, which are attributed to fine, the thermally stable MX particles (5–20 nm) and $M_{23}C_6$ carbides that provide effective dislocation pinning (Bajaj et al. 2020). A comprehensive evaluation by (Sham et al. 2022) demonstrated A709's superior overall performance across critical metrics, achieving the highest composite performance index among candidate alloys. A709's exceptional creep-fatigue resistance exhibits a fatigue life that is 3–5 times longer than that of 316H under representative thermal cycling conditions.

2.1.1 Heat Treatments for A709

The exceptional properties of A709 steel are achieved through carefully designed heat treatment protocols that optimize the precipitation microstructure for enhanced high-temperature performance. The standard sequence begins with solution annealing (SA) at 1050–1200°C, followed by rapid cooling to dissolve existing precipitates and homogenize the austenitic matrix, ensuring complete dissolution of carbides and carbonitrides while establishing a supersaturated solid solution.

Following solutionizing, A709 undergoes critical precipitation hardening around 750°C, which is an optimal temperature for promoting fine, coherent precipitates that provide substantial strengthening without compromising ductility (Sham et al. 2022). This treatment, typically conducted for 3–20 hours, promotes the nucleation and growth of thermally stable MX-type particles and $M_{23}C_6$ carbides with the optimal size distribution (5–50 nm) for maximum creep resistance. The treatment operates with favorable MX precipitation kinetics while avoiding excessive precipitate coarsening, resulting in a uniformly distributed precipitate structure that provides effective dislocation pinning during high-temperature creep exposure.

However, the cellular microstructure characteristic (Wanni et al. 2022) of additively manufactured A709 is expected to exhibit a different heat treatment response and mechanical properties compared to those of the conventional wrought alloy. The cellular/dendritic

solidification structure inherent to AM may influence the precipitation kinetics, precipitate distribution, and overall strengthening mechanisms. Limited information is currently available regarding the specific effects of heat treatment on the microstructural evolution and resulting mechanical properties of DED A709 steel, representing an important area for future research and development.

2.2 Grade 92 F/M Steel

F/M steels have emerged as leading candidates for next-generation nuclear reactors because of their superior mechanical, thermal, and radiation-resistance properties compared to those of austenitic stainless steels (Shrestha et al. 2015; Sridharan and Field 2019). Most critically, F/M steels demonstrate substantially reduced void swelling rates compared to their austenitic counterparts—essential for in-core structural components subjected to neutron fluences exceeding 10^{22} n/cm^2 (Sridharan and Field 2019).

G-92 steel represents a third-generation creep-resistant F/M steel engineered through strategic tungsten (W) substitution for molybdenum (Mo) in the G-91 baseline. This W-for-Mo substitution exploits tungsten's superior solid-solution strengthening and promotes the formation of thermodynamically stable precipitate phases, including fine $M_{23}C_6$ carbides and MX carbonitrides that provide enhanced creep resistance above 600°C (Klueh and Nelson 2007). Despite superior laboratory performance relative to that of G-91, G-92 has not achieved code qualification for nuclear applications. To the authors' knowledge, no systematic research exists on DED G-92 steel, representing a critical knowledge gap given the material's potential for nuclear applications and growing industrial interest in AM-fabricated reactor components.

2.2.1 Heat Treatments for G-92

F/M steels present unique characteristics when additively manufactured, exhibiting fine dendritic microstructures with residual stresses, segregation patterns, and non-equilibrium phases from rapid solidification. These characteristics necessitate careful heat treatment to achieve optimal mechanical properties and microstructural homogeneity.

A normalizing treatment at 1070°C serves multiple critical purposes, falling within the typical 1040–1180°C range for F/M steels to ensure the complete homogenization of the chemical composition and to dissolve the carbides formed during DED processing (Klueh and Nelson 2007). This treatment eliminates the as-built microstructural heterogeneities and refines the grain structure, with $M_{23}C_6$ carbides dissolving into the matrix while reducing micro segregation.

Subsequent tempering at 750°C for 0.5–4 hours provides precipitating strengthening via carbides and relieves residual stresses (El-Atwani et al. 2021). Microstructural evolution involves the transformation of fresh martensite into tempered martensite, accompanied by the precipitation of fine $M_{23}C_6$ carbides at the grain boundaries and Nb, V carbides (MX type) within grains, providing essential precipitation strengthening mechanisms.

For additively manufactured F/M steel, this approach eliminates AM-specific microstructural features, achieves properties like those of conventional wrought material, and reduces the anisotropy common in AM parts. Critical considerations include maintaining a protective atmosphere to prevent oxidation, ensuring adequate cooling rates for martensitic transformation, and achieving temperature uniformity for complex AM geometries.

3.0 Experimental Setup

3.1 Block Fabrication

For the uniaxial tensile testing of laser powder directed energy deposition (LP-DED) A709 and G-92 steels, test specimens were fabricated using process-optimized manufacturing parameters established through preliminary parameter development studies in FY 2024.The optimized processing parameters for A709 consisted of a laser power of 400 W, a scan velocity of 700 mm/min, and a constant hatch spacing, layer thickness, and powder feed rate maintained throughout the build process. The optimized processing parameters for G-92 were established at a laser power of 500 W, a scan velocity of 700 mm/min, and consistent hatch spacing, layer thickness, and powder feed rate. These processing conditions were selected to achieve high-density, defect-free builds with optimal microstructural characteristics for heat treatments and subsequent mechanical property evaluation. Figure 1 presents the A709 and G-92 test blocks successfully manufactured via LP-DED using the established processing protocols.

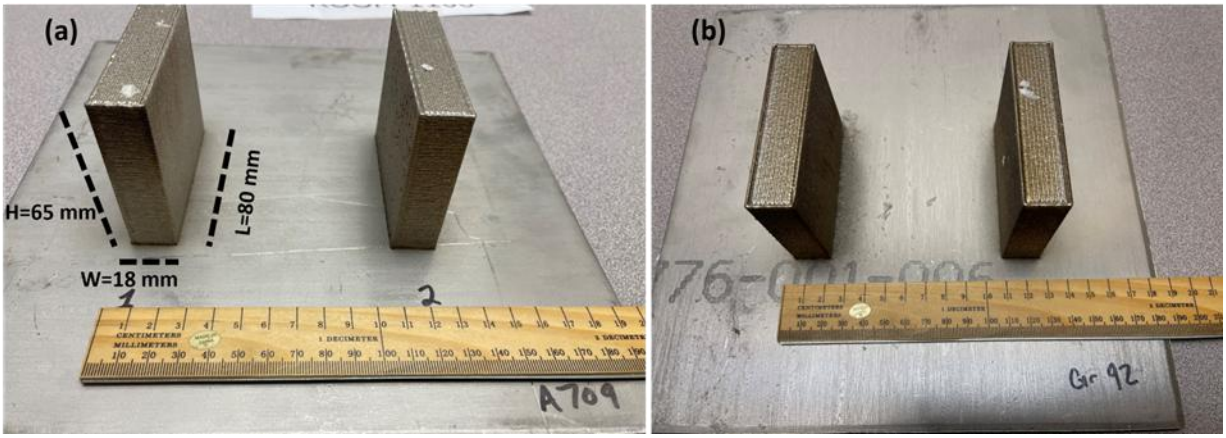

Figure 1. Blocks produced via LP-DED: (a) A709 and (b) G-92.

3.2 Heat Treatment

A709 and G-92 steels underwent the heat treatments specified in Tables 1 and 2, respectively. Heat treatments were performed using Vulcan model 3-550 and Thermolyne model 48025 furnaces.

Table 1. Heat treatment for A709 steel.

Heat Treatment	Temperature and Time	Quenching Medium
Solution Annealing (SA)	1150°C/1 h	Water Quench
Precipitation Treatment (PT)	775°C/10 h	Water Quench
SA+PT	1150°C/1 h + 775°C/10 h	Water Quench

Table 2. Heat treatment for G-92 steel.

Heat Treatment	Temperature and Time	Quenching Medium
Normalizing	1070°C/15 min	Water Quench
Tempering	775°C/45 min	Water Quench
Normalizing + Tempering (Dual Step)	1070°C/15 min + 775°C/45 min	Water Quench

3.3 Microstructural Characterization

An FEI Helios 660 Nanolab dual-beam focused ion beam (FIB) scanning electron microscope (SEM) equipped with energy-dispersive X-ray spectrometry (XEDS) was used to examine the cross-sectional phase constituents, microstructures, and compositions of G-92 samples. Grain orientation maps were acquired with a step size of 50 nm using a JEOL IT800 field emission SEM (FESEM) equipped with an Oxford Instruments Symmetry electron backscatter diffraction (EBSD) detector. Oxford Instruments AZtec Nanoanalysis v.4.3 was used for data acquisition in conjunction with AZtec Crystal v.3.3 for EBSD post-processing and analysis. The 15° misorientation criterion was used to distinguish the low-angle grain boundaries (LAGBs) and high-angle grain boundaries (HAGBs) (Cui et al. 2021). A 3 × 3 kernel with a threshold of 3° was used to process the kernel average misorientation (KAM) and geometrically necessary dislocation (GND) density maps. Detailed descriptions of the KAM and GND density calculations can be found in (Moussa et al. 2015; Konijnenberg et al. 2015; Pantleon 2008).

Transmission electron microscopy (TEM) lamellae from each sample were fabricated using an FEI Helios dual-beam FIB instrument. The microstructure was analyzed using a JEOL Grand Arm scanning tunneling electron microscope (STEM) at an acceleration voltage of 300 keV. Imaging was performed in bright-field (BF), high-resolution (HR), and high-angle annular dark-field (HAADF) modes. Elemental maps were acquired using STEM-coupled XEDS.

3.4 Mechanical Properties

3.4.1 Vickers Hardness Test

Vickers microhardness testing was performed using a Sun-Tec CM-802 AT microhardness tester equipped with ARS20 software for automated data acquisition. The testing parameters consisted of a load of 300 grams-force applied for 10 seconds per indentation. Each sample was evaluated using a minimum 5 × 5 indentation array with a 0.5 mm inter-indentation spacing to eliminate strain field interference between adjacent measurements, ensuring statistically reliable and reproducible hardness values. The instrument's calibration was verified prior to testing using Sun-Tec-certified reference standards (249HV0.3 and 297HV0.3) to confirm that the measured hardness values were within ±2% of the certified standard values, validating the measurement accuracy and traceability throughout the testing procedure.

3.4.2 Uniaxial Tensile Testing

The DED blocks were separated from the substrate build plate using wire electrical discharge machining (EDM) to ensure precise cutting without introducing thermal distortion or mechanical damage to the test material. Subsequently, both A709 and G-92 blocks underwent precision machining operations to extract standardized tensile test specimens according to established geometrical specifications.

The as-built block dimensions were length (L) = 80 mm, width (W) = 18 mm, and height (H) = 65 mm, providing sufficient material volume for multiple specimen extraction while maintaining consistent processing conditions throughout the build envelope. The precise tensile specimen geometry and dimensional tolerances are detailed in Figure 2, conforming to applicable ASTM testing standards for evaluating the uniaxial tensile properties of metallic materials.

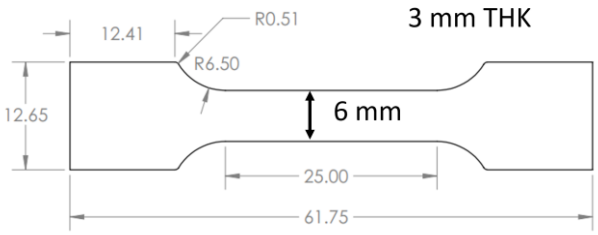

Figure 2. Dimensions of the tensile specimen utilized for tensile testing.

Block 1 underwent sectioning operations to produce four individual subblocks with a nominal thickness of 4 mm each, which were subsequently precision machined to extract 16 horizontally oriented (H) tensile specimens and 4 vertically oriented (V) tensile specimens relative to the build direction [Figure 3(b)]. Block 2 was similarly sectioned into three individual subblocks with a thickness of approximately 4 mm, from which 12 vertically oriented (V) specimens were machined exclusively [Figure 3(c)].

The specimen orientation nomenclature designates horizontal (H) specimens as those with their loading axis perpendicular to the build direction, while vertical (V) specimens have their loading axis parallel to the build direction. This extraction strategy yielded a total of 16 horizontal and 16 vertical tensile specimens from the combined blocks for each alloy system, providing adequate statistical sampling for mechanical property evaluation and the assessment of potential build-direction-dependent anisotropy in additively manufactured materials.

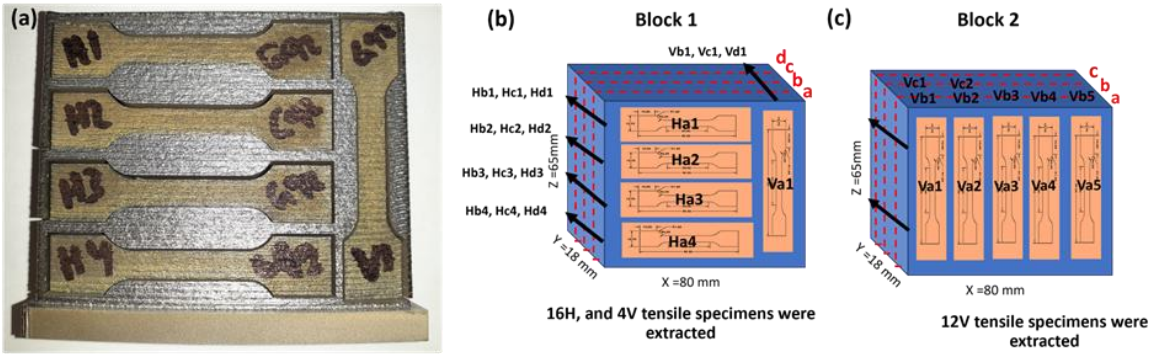

Figure 3. Extraction of tensile specimens from produced blocks. (a) Residual materials after extraction from one slice and schematics of the extraction procedure from (b) Block 1 and (c) Block 2.

Uniaxial tensile testing was performed using an MTS 10-kip (45 kN) servo-hydraulic testing machine with Instron Bluehill 2 software and an Epsilon One noncontact optical extensometer (Figure 4). The extensometer utilizes telecentric lenses for precise strain measurements up to a gauge length of 50 mm with a resolution of ±0.1 µm, maintaining accuracy despite the out-of-plane movement of the specimen.

The configuration included an Applied Test Systems (ATS) clamshell furnace with a 150 mm heating zone for elevated temperature testing and hydraulically actuated shoulder-loaded grips with ball-and-socket articulation for proper axial alignment. The Bluehill 2 software provided automated test control, real-time data acquisition, and systematic compilation of engineering stress–strain data throughout each test cycle.

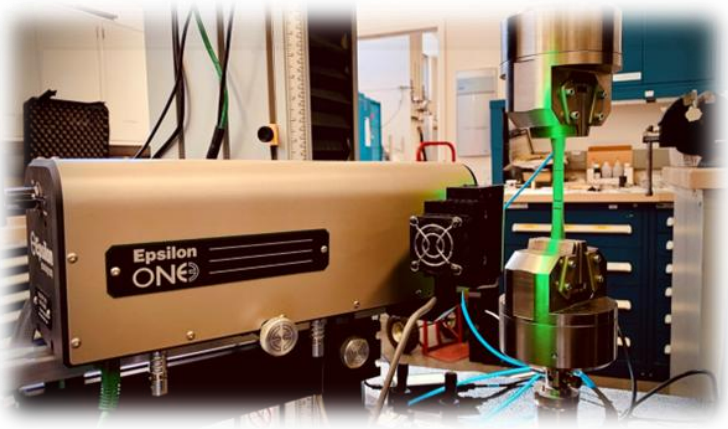

Figure 4. Noncontact extensometer setup.

3.5 Ion Irradiation Testing for A709

Preliminary irradiation testing was conducted to evaluate the radiation-induced microstructural evolution in AD DED A709. The experimental matrix encompassed four samples systematically irradiated to different displacement per atom (dpa) levels of 100, 200, 300, and 400 dpa, representing a range of radiation doses. Irradiation studies at a higher dose were performed to fundamentally evaluate the material response under extreme displacement damage conditions, investigating whether elemental segregation reaches equilibrium. The objective is also to understand and examine the element interactions with radiation-induced dislocations and void formation.

Ion irradiation experiments were performed at the Texas A&M University Ion Beam Laboratory using a controlled irradiation protocol specifically designed to simulate neutron radiation damage in nuclear reactor environments. Each sample, with an irradiated area of 5 mm × 5.5 mm, was subjected to bombardment with 3.5 MeV double-charged Fe^{2+} ions delivered at a beam current of 140 nA. The displacement damage rate was maintained at 1.7×10^{-3} dpa/s, representing an accelerated irradiation condition that enables efficient accumulation of radiation damage while maintaining temperature control. The irradiation temperature was precisely controlled at 575 ± 3°C, simulating elevated temperature service conditions typical of advanced nuclear reactor applications.

Critical experimental parameters were carefully maintained throughout the irradiation campaign to ensure data quality and reproducibility. The irradiation chamber was maintained under ultrahigh vacuum conditions at 8×10^{-8} Torr using a liquid nitrogen cold trap system, effectively eliminating atmospheric contamination and oxidation effects that could interfere with radiation damage mechanisms. This controlled environment ensures that the observed microstructural changes can be directly attributed to radiation-induced processes rather than environmental factors.

4.0 A709 Results and Discussion

To understand the high-temperature behavior and thermal stability of DED A709, systematic heat treatment investigations were conducted according to the protocols detailed in Table 1. These heat treatment regimens were specifically designed to optimize the precipitation microstructure and relieve the residual stress. The characterization program focused on quantifying the formation and distribution of precipitates and the development of mechanical properties following the heat treatment conditions. Uniaxial tensile testing was performed at ambient temperature and 550°C to evaluate the heat treatment effects on the YS, UTS, and total elongation. The elevated temperature testing represents sodium-cooled fast reactor (SFR) operating conditions, enabling the assessment of temperature-dependent deformation mechanisms and the validation of material performance under service-relevant conditions.

4.1 Microstructure Analysis

A detailed analysis of different heat treatment conditions for A709 austenitic stainless steel has been systematically carried out, encompassing AD, SA, precipitation treatment (PT), and the combined solution annealing plus precipitation treatment (SA+PT) conditions.

4.1.1 As-Deposited Condition

Figure 5 shows backscattered SEM images of the AD A709 steel across multiple magnifications and orientations, revealing the complex three-dimensional microstructural architecture characteristic of the DED process. The images obtained along the build direction in Figures 5(a–c) show the grain size distributions as well as the solidification cell walls with a thickness of ~2–3 μm within the grains. These fine-scale features are formed during rapid cooling from the molten state, and compositional segregation of the alloying elements occurs in the intercellular regions. Similarly, the perpendicular orientation images Figures 5(d–f) provide a similar cross-sectional perspective of the cellular/dendritic solidification structure. The grain size of the AD microstructure was observed to be 10–50 μm. This comprehensive microstructural documentation across different orientations and magnifications establishes the baseline understanding of the AD condition, which is essential for subsequent heat treatment optimization and for correlating the processing parameters with the final mechanical properties.

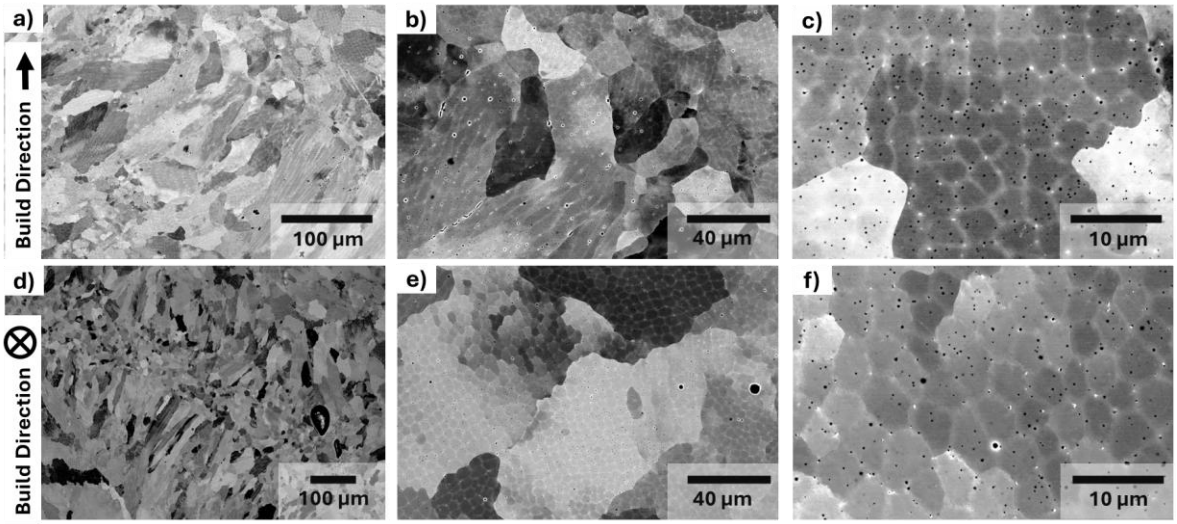

Figure 5. Backscattered SEM images of AD DED A709 steel at different magnifications. Images taken (a–c) along and (d–f) perpendicular to the build direction.

Figure 6 presents a comprehensive EBSD characterization of as-deposited DED A709 steel, systematically comparing microstructural features along two orientations relative to the build direction. This dual-orientation analysis is particularly important where the layer-by-layer deposition creates inherent directional dependencies in microstructure and properties. The inverse pole figure (IPF) + image quality (IQ) maps in Figure 6 (a,f) reveal the spatial distribution of crystallographic orientations and grain morphologies, highlighting any preferential grain growth or epitaxial solidification effects that may differ between the two orientations. The kernel average misorientation (KAM) maps Figure 6 (b,g) quantify local plastic deformation and residual strain distributions, which are critical for understanding the thermal stress effects during the rapid heating and cooling cycles of DED processing. The grain reference orientation deviation (GROD) maps Figure 6 (c,h) complement this analysis by illustrating intragranular misorientation patterns and subgrain boundary development. The pole figures (PF) in Figure 6 (d,i) and IPF in Figure 6 (e,j) provide statistical texture analysis, revealing no preferred orientations was developed during solidification and subsequent thermal cycling. This

comprehensive microstructural characterization is essential for predicting the anisotropic mechanical behavior and performance reliability of DED A709 steel components.

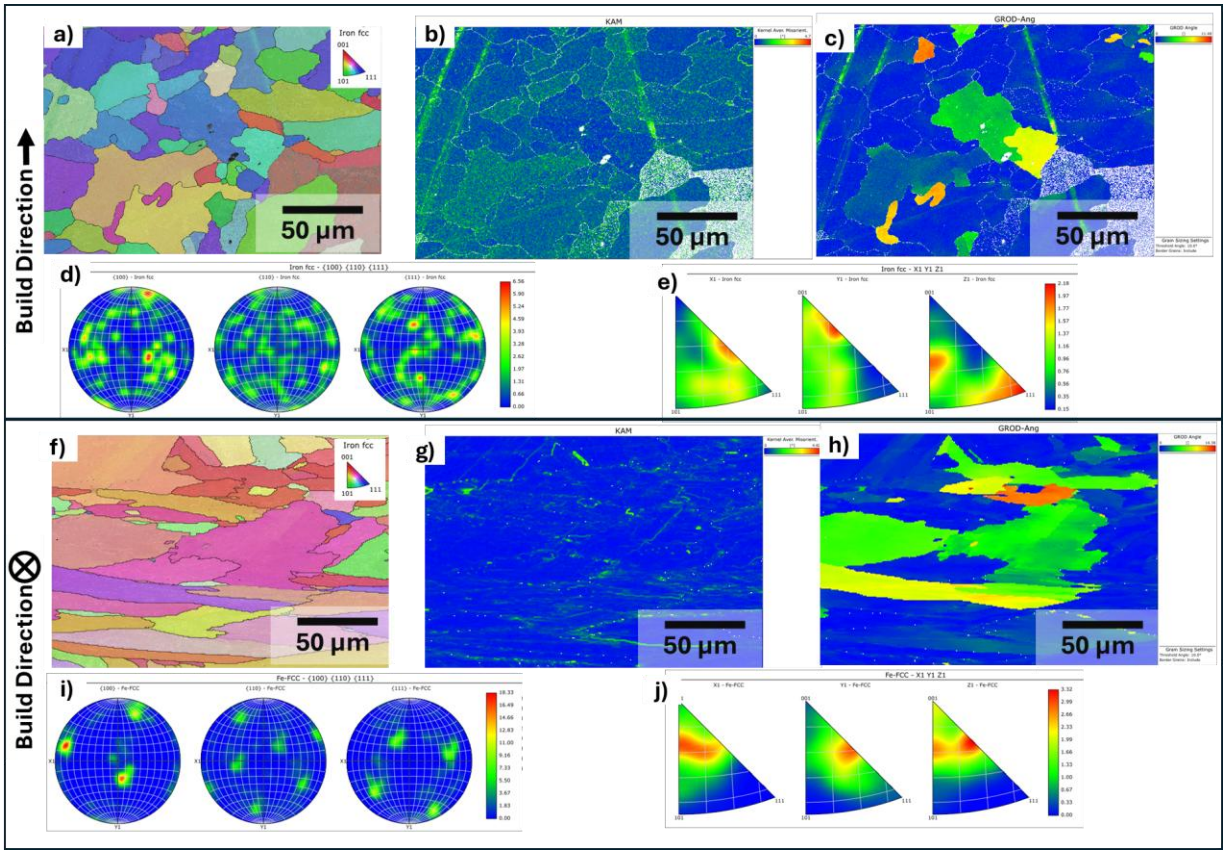

Figure 6. Orientation microscopy of as deposited DED A709 Steel showing (a-e) analysis along build direction and (f-j) analysis parallel to build direction: IPF +IQ maps (a,f), KAM maps (b,g), GROD maps (c,h), PF (d,i), and IPF (e,j).

HAADF-STEM characterization of the AD DED A709 steel in Figure 7 provides detailed nanoscale insight into the precipitation behavior and grain boundary chemistry inherent to the rapid solidification conditions of the DED process. The STEM images in Figures 7(a–b) reveal the presence of grain boundary precipitates that formed during the thermal cycling experienced during layer-by-layer deposition, demonstrating the material's tendency to develop secondary phases even in the AD condition without deliberate heat treatment. The complementary XEDS elemental maps in Figure 7(c) of the region shown in Figure 7(b) provide critical compositional information, revealing complex elemental distributions along the grain boundaries with the identification of NbC-type nodules distributed along chromium carbide phases. This precipitate morphology and composition are significant as they represent carbide-forming elements (Nb, Cr) or $M_{23}C_6$-type precipitates that have segregated to grain boundaries during solidification, potentially affecting subsequent heat treatment response and mechanical properties.

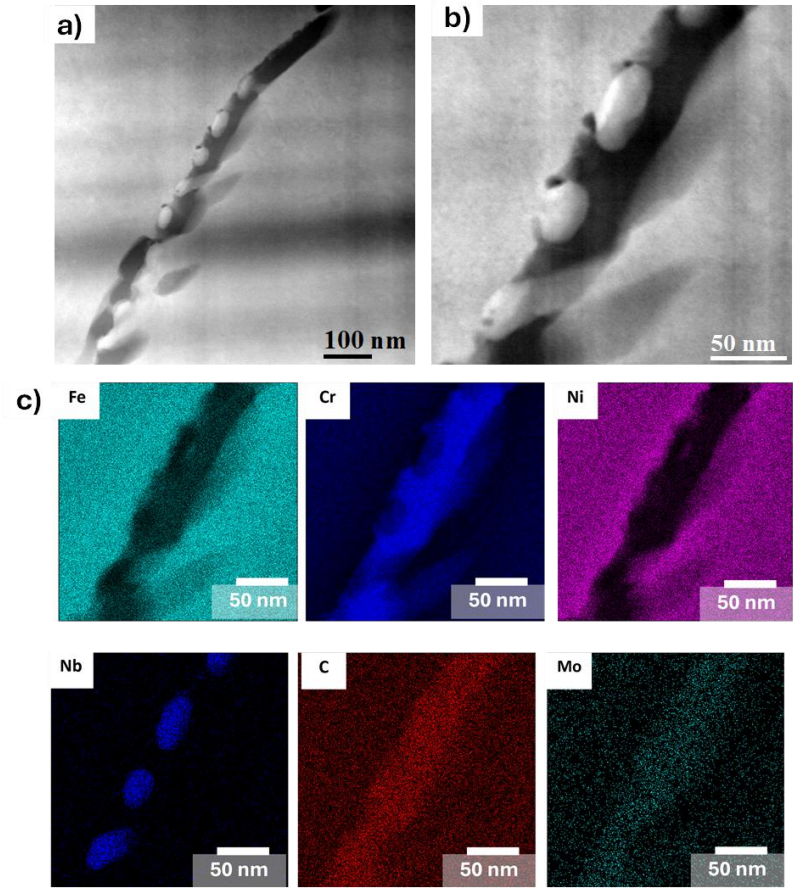

Figure 7. HAADF-STEM characterization of AD DED A709 steel. (a–b) HAADF-STEM images revealing grain boundary precipitates. (c) EDS maps of the region shown in (b), revealing the elemental distributions in the grain boundaries with NbC-type nodules along the chromium carbide phase.

4.1.2 Solution Annealing

SEM and EBSD characterization of DED A709 steel following the SA heat treatment demonstrates the effective microstructural homogenization achieved through controlled thermal processing. The backscattered SEM images in Figures 8(a–c) clearly illustrate the dissolution of the characteristic cellular solidification structure observed in the AD condition, with the previously distinct cell walls becoming progressively less defined as the SA treatment promotes the diffusion-controlled homogenization of the segregated alloying elements. The decreased chemical inhomogeneity along the former cell boundaries indicates the successful redistribution of elements that had partitioned during the rapid solidification of the DED process, resulting in a more chemically uniform austenitic matrix suitable for subsequent precipitation heat treatments. The EBSD inverse pole figure (IPF) map in Figure 8(d) reveals the crystallographic grain structure of the heat-treated condition, showing the grain size distribution that occurred at the SA temperature. This transformation from the fine cellular solidification structure to a more homogeneous grain structure represents a critical step in optimizing the material for nuclear applications, as the elimination of compositional gradients and the establishment of controlled grain boundaries are essential for achieving consistent mechanical properties and predictable high-temperature performance.

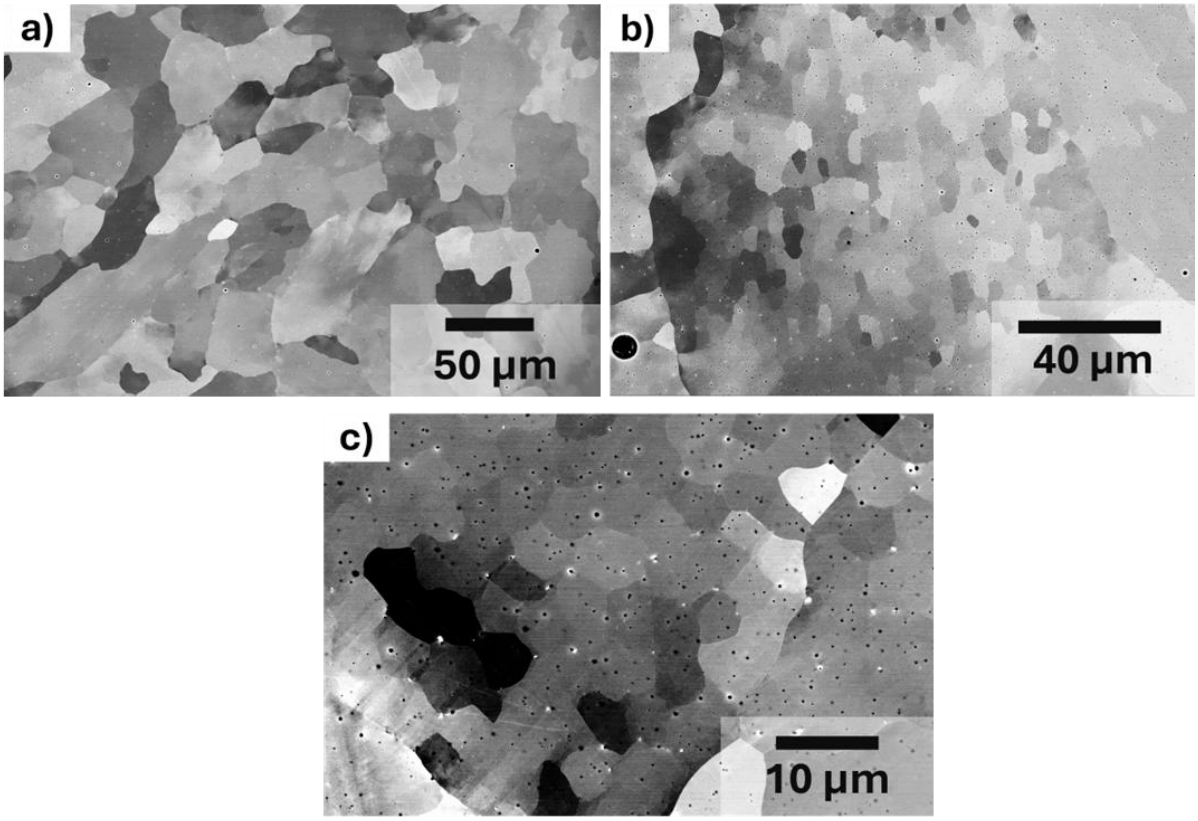

Figure 8. Backscattered SEM images and EBSD map of DED A709 steel after the SA heat treatment. (a–c) Images showing the dissolution of cell walls and the decreased chemical inhomogeneity along the cell walls. (d) IPF map of the heat-treated condition showing the grain distribution.

Figure 9 demonstrates the microstructural transformation of DED A709 steel following solution annealing treatment through directional EBSD analysis along and perpendicular to the build direction. The solution annealing process is expected to homogenize the microstructure and relieve residual stresses that developed during the as-deposited condition. The IPF+IQ maps in Figure 9 (a,f) illustrate grain structure evolution, while the KAM maps in Figure 9 (b,g) reveal the effectiveness of stress relief achieved through SA, when compared to KAM analysis of AD samples. The GROD maps in Figure 9 (c,h) show changes in intragranular deformation patterns compared to the as-deposited state. The crystallographic texture analysis through pole figures (d,i) and inverse pole figures (e,j) quantifies how the solution annealing treatment affects preferred orientations, and it was revealed that no change in texture occurred via SA. This comparative directional analysis provides crucial insight into the thermal treatment's ability to optimize microstructural homogeneity and reduce processing-induced anisotropy.

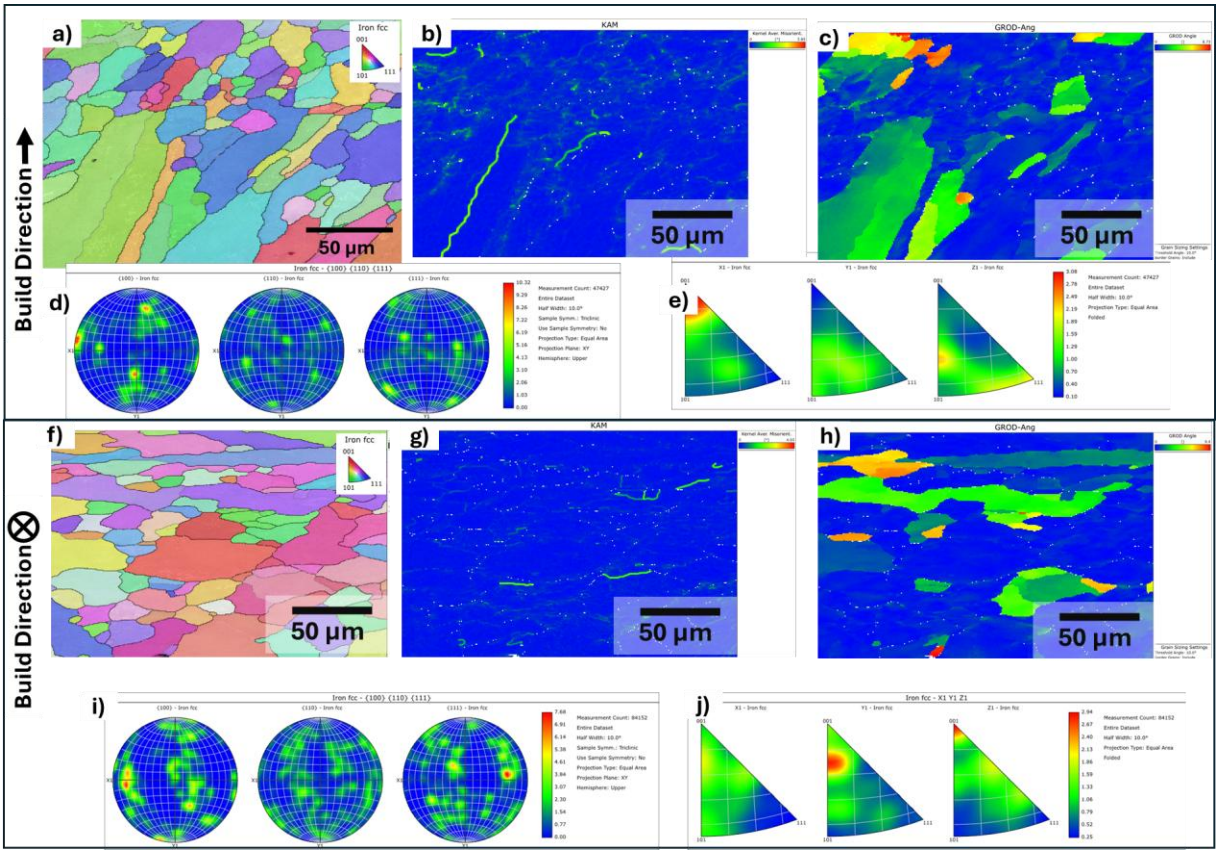

Figure 9: Orientation microscopy of solution annealed DED A709 Steel showing (a-e) analysis along build direction and (f-j) analysis parallel to build direction: IPF maps (a,f), KAM maps (b,g), GROD maps (c,h), pole figures (d,i), and inverse pole figures (e,j).

The TEM images in Figures 10(a–b) reveal a precipitate-free austenitic matrix, confirming the successful achievement of a supersaturated solid solution condition. The absence of carbide and carbonitride precipitates confirms that the SA temperature and time were sufficient to dissolve the strengthening phases that may have formed during the DED process or existed in the starting powder material, creating the desired supersaturated condition necessary for subsequent controlled precipitation heat treatments. However, the presence of oxide particles within the matrix indicates that these thermodynamically stable phases were not dissolved during the SA treatment, likely consisting of aluminum oxide, titanium oxide, or complex oxide phases that form during the high-temperature DED process. These oxide particles, while generally stable and not significantly affected by typical heat treatment temperatures, can serve as heterogeneous nucleation sites for subsequent carbide precipitation and may influence the final precipitate distribution during annealing treatments. The clean, precipitate-free matrix condition demonstrated in these TEM images represents the optimal starting point for controlled precipitation heat treatments designed to develop the fine, uniformly distributed $M_{23}C_6$ carbides and MX carbonitrides essential for achieving the superior high-temperature creep resistance and mechanical properties.

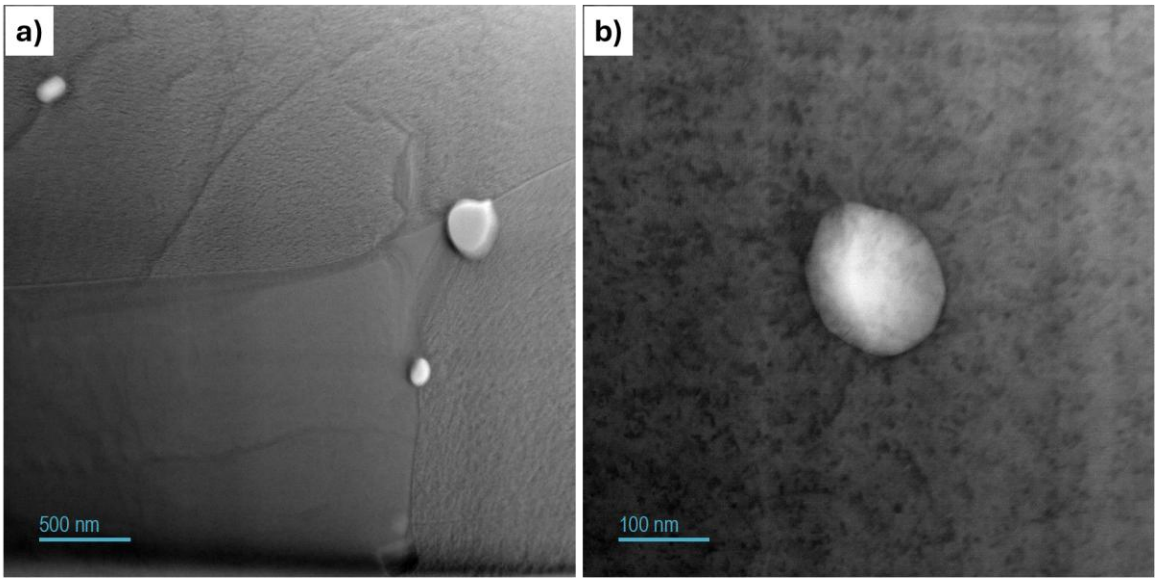

Figure 10. TEM images of DED A709 steel after the SA heat treatment. (a–b) Images showing a matrix free of precipitates with the presence of oxide particles.

4.1.3 Precipitation Treatment

SEM characterization of DED A709 steel following the PT heat treatment reveals a complex microstructural evolution that differs significantly from that for the SA-treated DED A709 steel, demonstrating the material's response to controlled thermal aging designed to develop strengthening precipitates. The low magnification SEM image in Figure 11(a) shows that the cellular solidification structure remains largely intact after the PT heat treatment, indicating that the lower temperature and shorter time of the PT were insufficient to eliminate the AD cellular morphology, unlike the homogenization achieved during SA. The formation of distinct grain boundary precipitates, clearly visible in the higher magnification view in Figure 11(b), confirms the effectiveness of the precipitation heat treatment in promoting carbide and carbonitride formation at high-energy sites. Figures 11(c–d) provide critical insight into the dislocation–precipitate interactions at cell wall boundaries, where the residual strain energy from the DED process creates preferential nucleation sites for precipitate formation, resulting in a heterogeneous distribution that could influence the mechanical properties. The SEM-EDS elemental maps in Figure 11(e) reveal the persistent chemical inhomogeneity within the matrix, with significant segregation of Mo, Cr, and Nb concentrated at cell wall boundaries, indicating that the PT time and temperature were insufficient to achieve complete chemical homogenization.

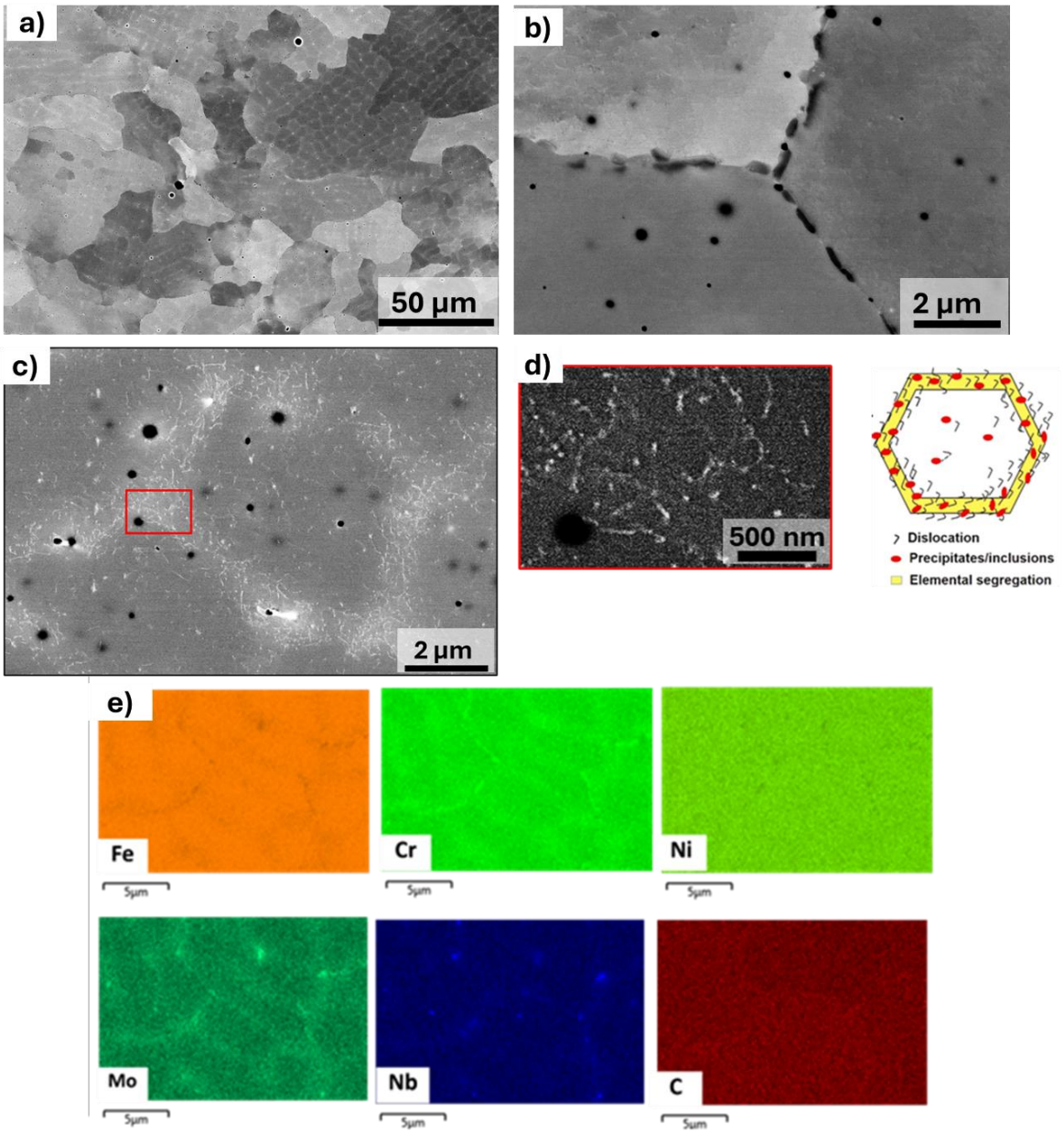

Figure 11. SEM characterization of DED A709 steel after the PT heat treatment. (a) Low magnification SEM image showing intact cell walls and grain boundary precipitates. (b) Higher magnification view of grain boundary precipitates. (c) High magnification SEM image revealing dislocations and precipitates at cell wall boundaries. (d) Magnified view of the area enclosed by the red box in (c) showing dislocation and precipitate details with a schematic explanation. (e) SEM-EDS maps showing the chemical inhomogeneity in the matrix with Mo, Cr, and Nb segregation at cell walls.

Figure 12 presents EBSD characterization of PT DED A709 steel, examining microstructural features in both build direction and transverse orientations. The post-treatment processing appears to have similar original DED microstructure, as evidenced through the IPF+IQ maps in Figure 12(a,f). The KAM maps in Figure 12(b,g) indicate similar stain distribution compared to AD condition and significantly higher strain distribution compared to that of SA condition. The

GROD analysis in Figure 12(c,h) reveals how intragranular misorientation patterns have evolved following post-treatment, while the texture analysis via pole figures Figure 12 (d,i) and inverse pole figures in Figure 12(e,j) demonstrates no impact on crystallographic preferred orientations.

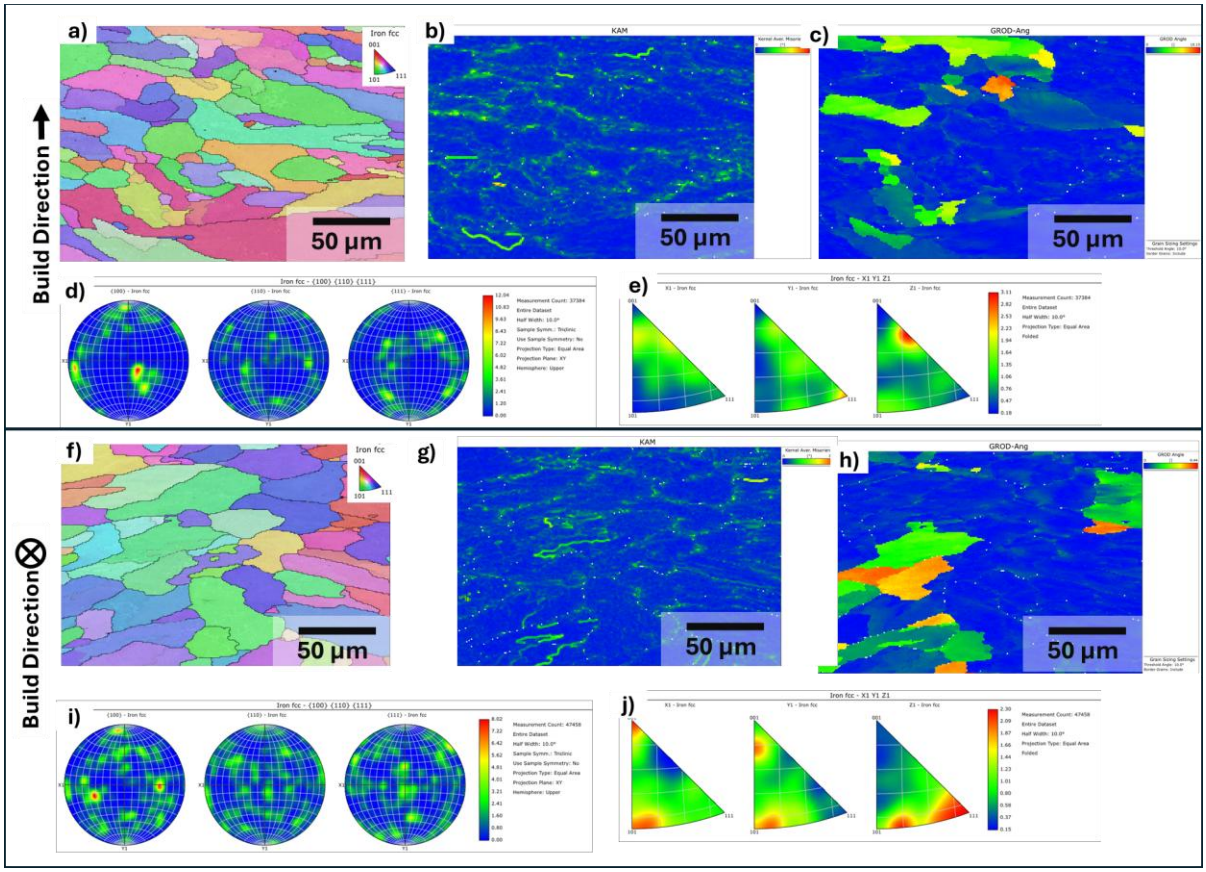

Figure 12: Orientation microscopy of PT DED A709 steel showing (a-e) analysis along build direction and (f-j) analysis parallel to build direction: IPF maps (a,f), KAM maps (b,g), GROD maps (c,h), pole figures (d,i), and inverse pole figures (e,j).

STEM analysis of the complete lamella in Figure 13 reveals substantial microstructural heterogeneity in the DED A709 steel following PT. The large field-of-view montage captures the complex spatial distribution of dislocations and precipitates. The blue inset reveals how nanometer-scale precipitates directly interact with dislocations to create critical strengthening effects. This precipitate–dislocation coupling serves as the primary strengthening mechanism for elevated temperature applications. The orange inset focusing on the cell wall precipitates reveals the preferential nucleation and growth of carbides and carbonitrides at the boundaries of the original cellular solidification structure, where compositional segregation and the residual strain energy from the DED process create favorable thermodynamic and kinetic conditions for precipitation. This heterogeneous precipitate distribution, while providing strengthening, may also introduce localized stress concentrations and potential anisotropy in the mechanical properties.

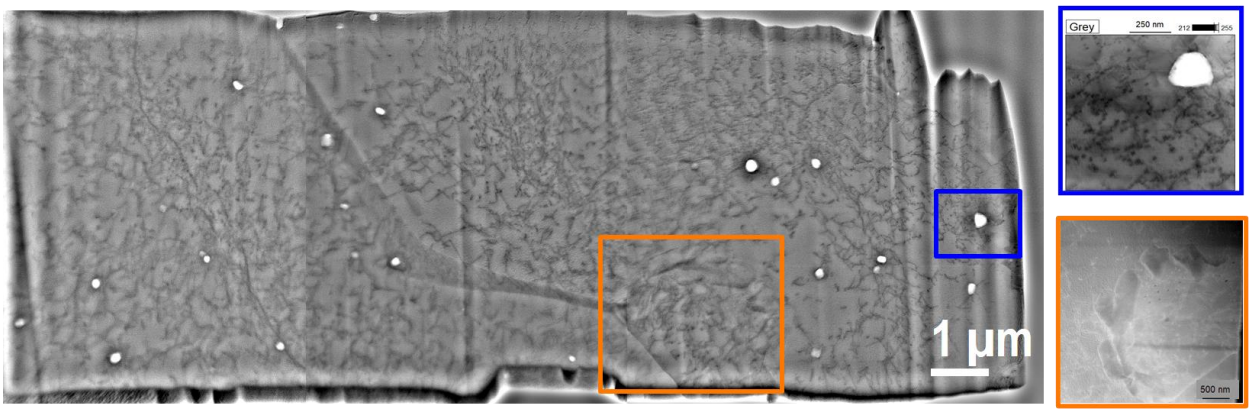

Figure 13. TEM montage of an entire lamella of DED A709 steel after the PT heat treatment, showing the distribution of dislocations and precipitates over a large field of view. The blue and orange insets show the nanoscale precipitate–dislocation interactions and cell wall precipitates, respectively.

Figures 14(a–b) show TEM-EDS elemental maps of DED A709 steel following the PT and reveal the formation of two distinct precipitate populations with different compositions, morphologies, and spatial distributions that contribute to the material's strengthening mechanisms. Figure 14(a) shows cell wall precipitates with substantial Cr, carbon (C), and Mo enrichment, consistent with $M_{23}C_6$ carbide precipitation. These relatively coarse precipitates, while providing some strengthening through precipitation hardening mechanisms, may also serve as potential crack initiation sites because of their locations at microstructural discontinuities and their brittle nature compared to the austenitic matrix. In contrast, Figure 14(b) reveals nanoscale MX-type precipitates distributed throughout the matrix, showing primary enrichment in niobium (Nb). These precipitates are identified as NbC or Nb(C, N) carbonitrides that form coherently within the austenitic grains. Their superior strengthening effectiveness results from three key characteristics: fine size, high number density, and strong coherency strains that effectively impede dislocation motion. This dual precipitate population—$M_{23}C_6$ Cr-rich carbides at cell boundaries and MX Nb-rich carbonitrides distributed within the matrix—creates a complex microstructural architecture requiring careful heat treatment optimization. The goal is to achieve superior high-temperature creep resistance and mechanical properties for SFR applications while preserving adequate ductility and toughness.

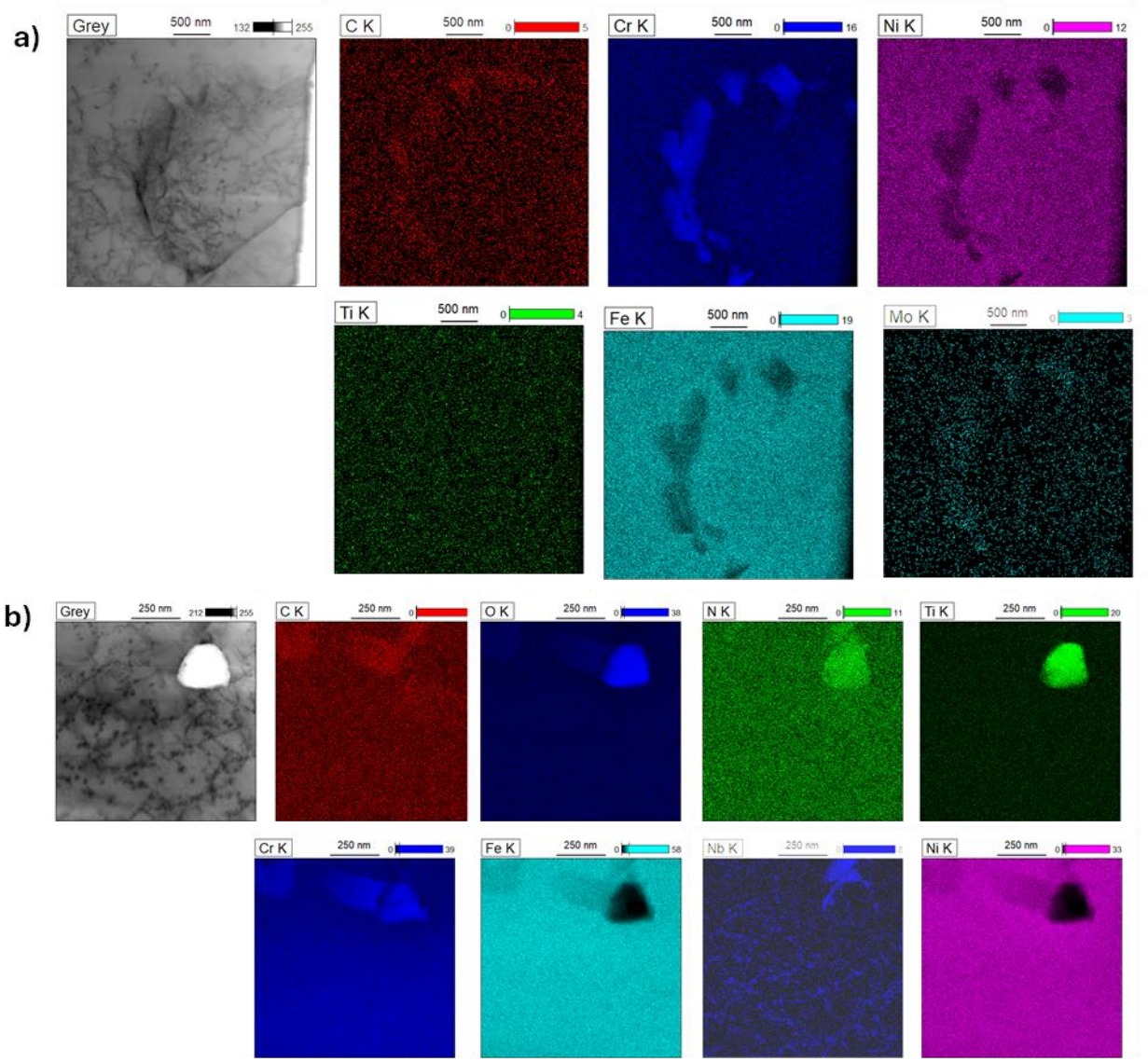

Figure 14. TEM-EDS maps of DED A709 steel after the PT heat treatment. (a) Chemical composition of cell wall precipitates showing enrichment in Cr, C, and Mo. (b) Nanoscale MX-type precipitates in the matrix enriched primarily in Nb.

4.1.4 SA+PT Treatment

Microstructural characterization of DED A709 steel demonstrates the benefits of SA+PT for nuclear applications. Figures 15(a–c) show backscattered SEM images revealing microstructural changes through SA+PT. The SA step dissolved the cellular solidification structure and eliminated the chemical inhomogeneity along the cell walls. The subsequent PT created $M_{23}C_6$ precipitates at the grain boundaries rather than at the original cell wall positions. Figure 15(d) shows the IPF map displaying the grain structure achieved through the combined treatment. This combined treatment significantly improves upon the PT-only conditions by producing uniform grain boundary precipitates after homogenization, in contrast with the heterogeneous cell wall precipitates that develop in the chemically segregated AD structures. The resulting microstructural architecture combines chemical homogenization with controlled precipitation at thermodynamically favorable sites, eliminating compositional gradients while

developing uniform strengthening precipitates. Note: MX-type precipitates cannot be resolved at the SEM scale and are therefore not discussed in this SEM analysis.

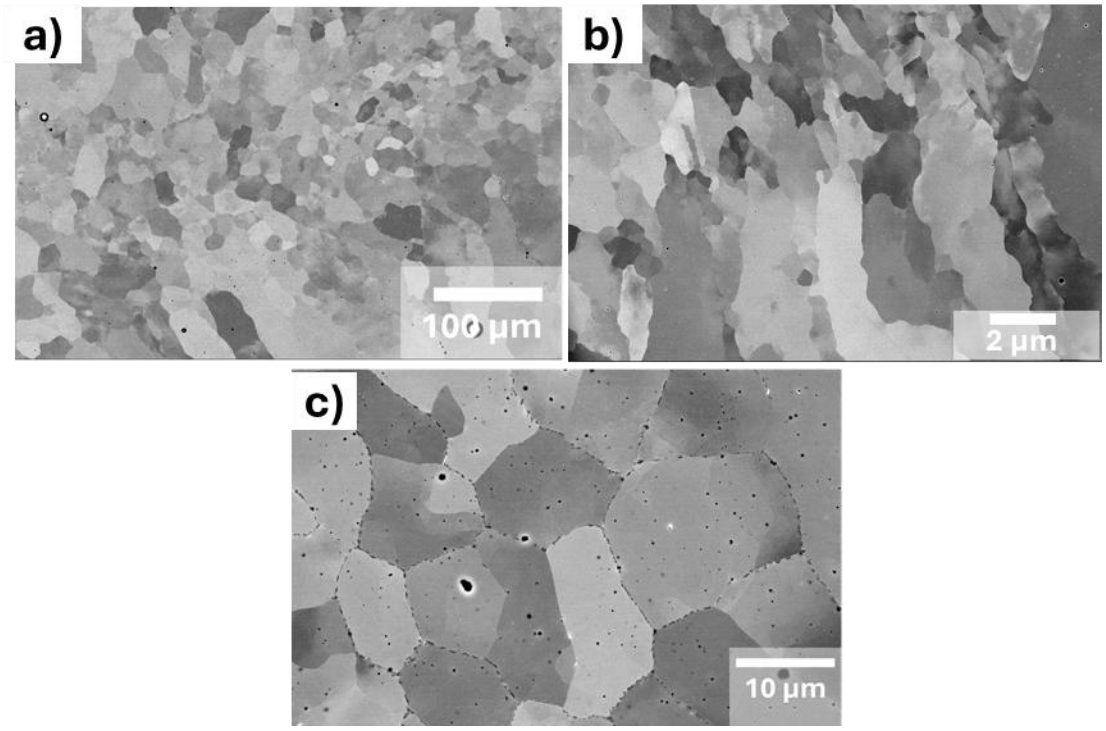

Figure 15. Backscattered SEM images and EBSD map of DED A709 steel after SA+PT. (a–c) Images showing the dissolution of cell walls and decreased chemical inhomogeneity along the cell walls, with grain boundaries decorated with precipitates.

Figure 16 presents a comprehensive orientation microscopy analysis of SA+PT condition, examining the crystallographic characteristics in two key orientations relative to the build direction. The analysis includes five complementary techniques applied both along the build direction in Figure 16(a-e) and parallel to it in Figure 16(f-j). Similar to SA condition, the KAM map shows the reduction of strain distribution due to inclusion of SA in this dual heat treatment.

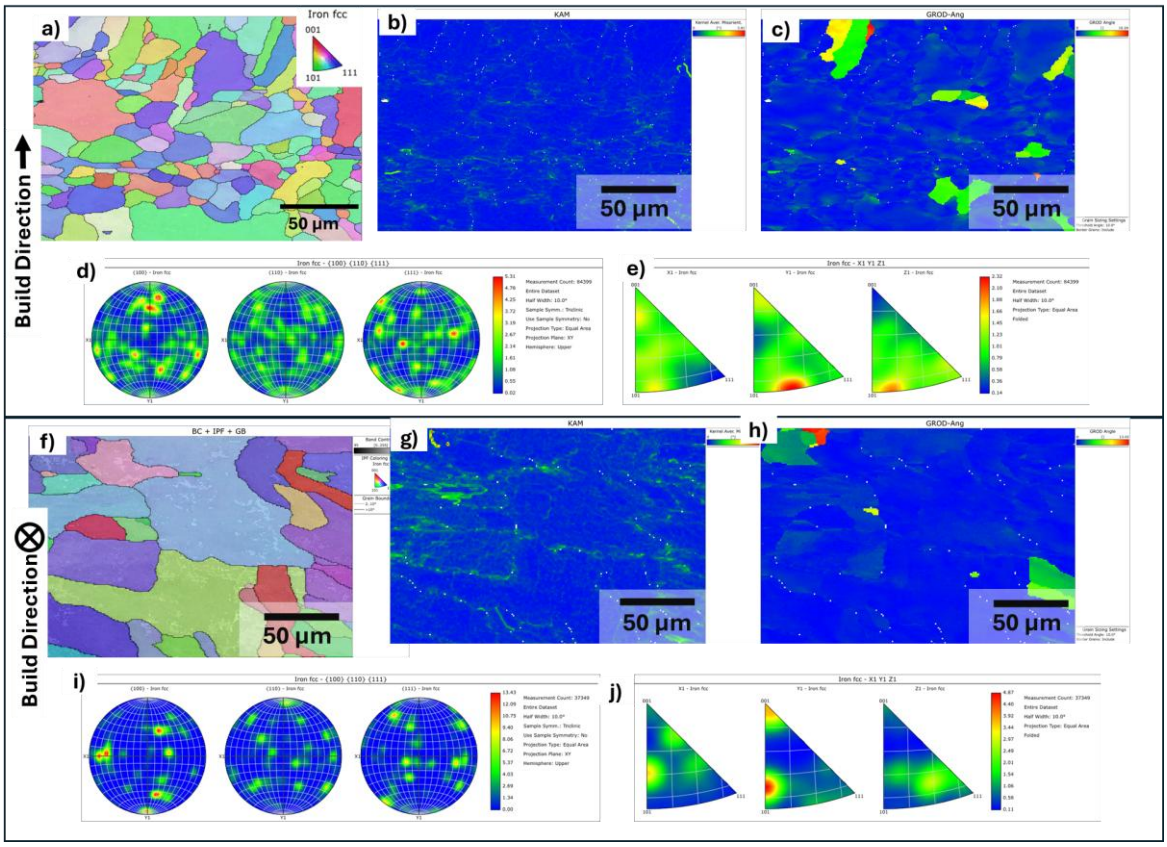

Figure 16: Orientation microscopy of SA+PT DED A709 steel showing (a-e) analysis along build direction and (f-j) analysis parallel to build direction: IPF maps (a,f), KAM maps (b,g), GROD maps (c,h), pole figures (d,i), and inverse pole figures (e,j).

HAADF-STEM characterization reveals the optimized microstructural development achieved through SA+PT in DED A709 steel. Figure 17(a) shows the reduced dislocation density in the matrix compared to that for the PT-only treatment, demonstrating that SA effectively relieved the residual strain energy from the DED process while maintaining adequate dislocation networks for strengthening after the subsequent PT. Figure 17(b) shows grain boundary precipitates that formed preferentially at recrystallized grain boundaries during the PT phase. These precipitates exhibit a more uniform distribution and composition compared to the heterogeneous cell wall precipitates observed in PT-only conditions, reflecting the benefits of prior chemical homogenization during SA. Figures 17(c–d) show matrix regions containing nanoscale MX precipitates interacting with dislocations through coherent interfaces. These dislocation–precipitate interactions provide critical strengthening mechanisms while benefiting from the more uniform chemical composition achieved through the initial SA step. SA+PT successfully combines dislocation recovery, chemical homogenization, and controlled precipitation to create a balanced microstructure with reduced residual stresses and a uniform precipitate distribution—essential characteristics for reliable nuclear reactor performance.

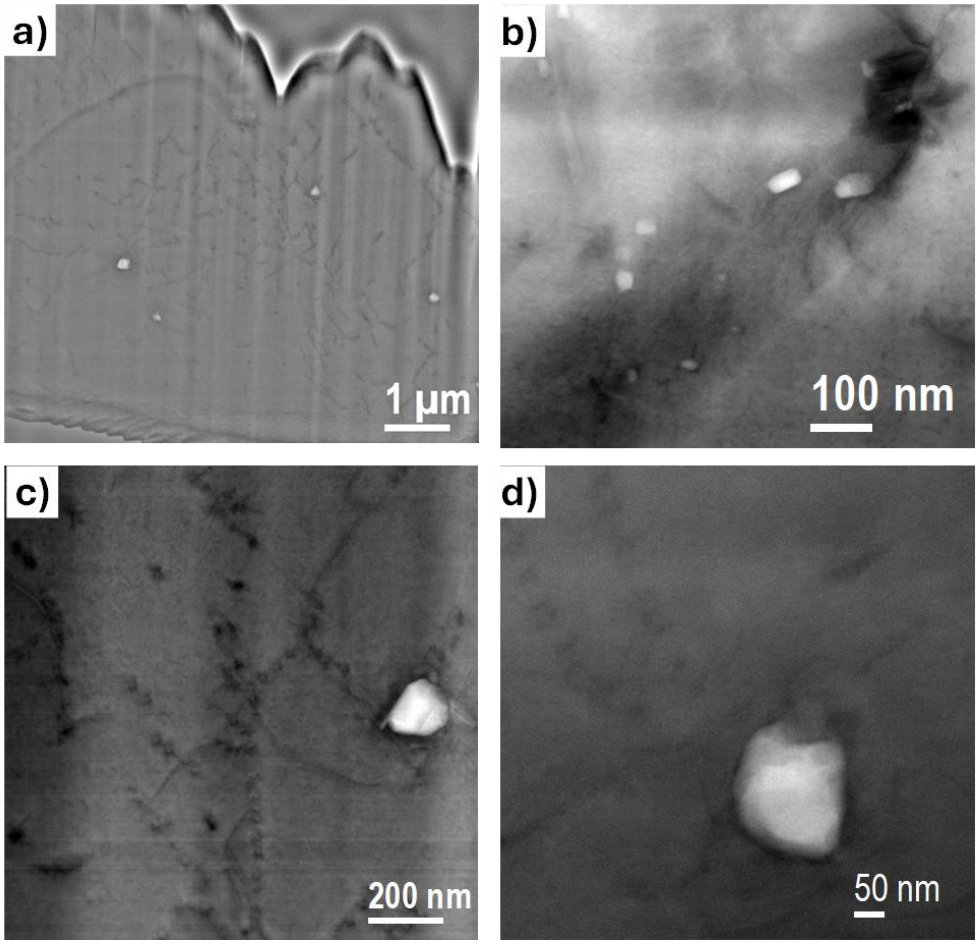

Figure 17. HAADF-STEM characterization of DED A709 steel after SA+PT. (a) Presence of dislocations in the matrix, which are reduced in density compared to the that of PT heat-treated condition. (b) Grain boundary precipitates. (c–d) Matrix showing the interactions between dislocations and nanoscale MX precipitates.

STEM-EDS characterization provides detailed insight into the matrix precipitation behavior achieved in DED A709 steel following SA+PT. Figure 18(a) shows an STEM image revealing the fine-scale precipitates distributed throughout the austenitic matrix, appearing as bright contrast features. Figure 18(b) shows the corresponding chemical maps, confirming that these precipitates are significantly enriched in Nb, identifying them as MX-type precipitates, likely NbC or Nb(C, N) carbonitrides. The uniform distribution and fine size of these Nb-rich precipitates demonstrate the effectiveness of SA+PT, where the initial SA created a homogeneous matrix composition followed by controlled precipitation during aging that promoted coherent MX precipitate formation.

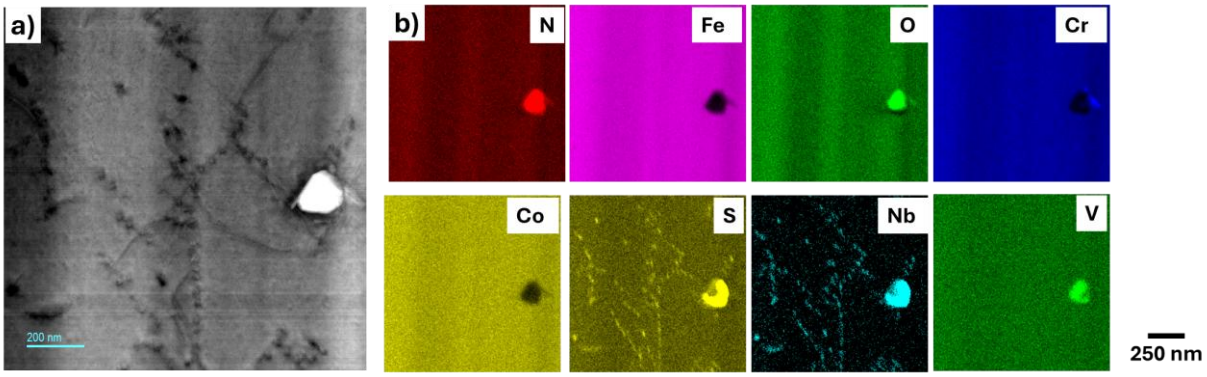

Figure 18. TEM-EDS maps of DED A709 steel after the SA+PT heat treatment. (a) HAADF-STEM image and (b) corresponding chemical maps of the matrix showing MX precipitates enriched in Nb.

4.2 Mechanical Properties

4.2.1 Vickers Hardness

The Vickers hardness measurements presented in Figure 19 reveal systematic trends that directly correlate with the microstructural evolution under different thermal processing conditions. The AD condition exhibited the highest hardness value of approximately 220 HV, attributed to the combination of a high dislocation density from rapid DED solidification, a fine cellular structure, and the nonequilibrium precipitates formed during rapid cooling. This elevated hardness results from multiple strengthening mechanisms including Hall–Petch grain boundary strengthening, dislocation strengthening, and precipitation hardening from fine-scale phases.

The SA treatment produced the lowest hardness of approximately 190 HV, representing an ~14% reduction from that of the AD condition. This decrease primarily results from the substantial reduction in the dislocation density at the elevated SA temperature, combined with precipitate dissolution that eliminates precipitation strengthening effects and relieves residual stresses.

The PT achieved an intermediate hardness of approximately 205 HV, while the combined SA+PT treatment reached 195 HV. These intermediate values reflect the balance between dislocation recovery and controlled precipitate formation. The SA+PT condition demonstrates optimal microstructural development through uniform, fine-scale strengthening precipitates in a recrystallized matrix, eliminating the microstructural heterogeneities present in the AD condition while maintaining adequate hardness.

The progressive hardness reduction from AD (220 HV) → PT (205 HV) → SA+PT (195 HV) → SA (190 HV) quantitatively demonstrates the effectiveness of each heat treatment in modifying the strengthening mechanisms active in DED A709 steel.

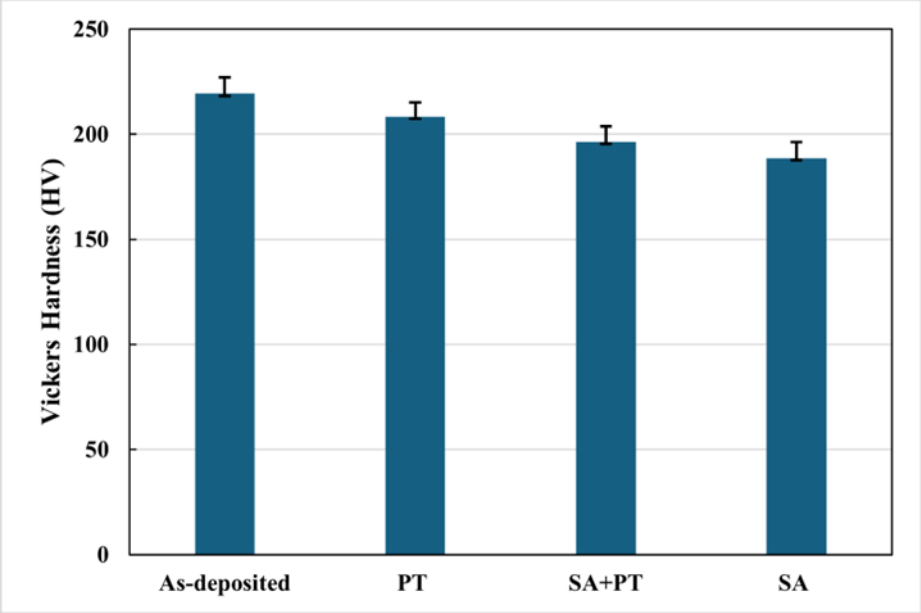

Figure 19. Vickers hardness of LP-DED A709 steel before and after heat treatment.

4.2.2 Uniaxial Tensile Testing

Figure 20 presents an evaluation of the mechanical properties of specimens extracted in two orientations relative to the build direction to assess the potential anisotropic behavior characteristic of AM processes. Figure 20 presents the engineering stress–strain behavior of DED A709 steel in both the AD condition and following the SA+PT heat treatment, with tensile testing conducted at RT. Quantitative data are provided in Table 3.

The AD mechanical behavior reveals significant directional anisotropy in the tensile properties. Horizontally extracted specimens (AD_Hd1 and AD_Ha4, red solid lines) demonstrate superior performance with an average YS of 602 MPa, UTS of 844 MPa, and total elongation of 35%.

Vertically extracted specimens (AD_Va1 and AD_Vd1, red dashed lines) exhibit lower mechanical properties with an average YS of 529 MPa and UTS of 760 MPa while maintaining a similar elongation. This represents a ~12% reduction in the YS and an ~10% reduction in the UTS compared to those of the horizontal-orientation specimens.

Notably, individual specimens from each orientation showed reproducible mechanical properties (Table 3), with consistent YS, UTS, and elongation values within both horizontal and vertical extraction groups, indicating uniform material quality for each build direction.

The SA+PT heat treatment effects are shown by the pink curves in Figure 20, revealing a significant reduction in strength. SA+PT_Ha1 achieved an YS of 410 MPa, a UTS of 746 MPa, and an elongation of 39%, while SA+PT_Vc1 showed an YS of 371 MPa, a UTS of 666 MPa, and an elongation of 41%. This represents an ~32%–44% reduction in the YS compared to that of the AD condition, while the directional anisotropy persists. The mechanical anisotropy persisted even after the SA+PT heat treatment, indicating that the combined thermal processing was insufficient to eliminate the directional microstructural features established during AM.

The as-received (AR) wrought A709 steel [Wrought_AR, black line in Figure 20] achieved a YS of 419 MPa, a UTS of 849 MPa, and an elongation of 41 %. The AD DED horizontal specimens demonstrated a 44% higher YS than that of the wrought material while maintaining a comparable UTS and slightly lower ductility. This enhanced YS in the AM condition can be attributed to the fine microstructural features, high dislocation density, and residual stress state characteristic of the rapid solidification and thermal cycling experienced during the DED process.

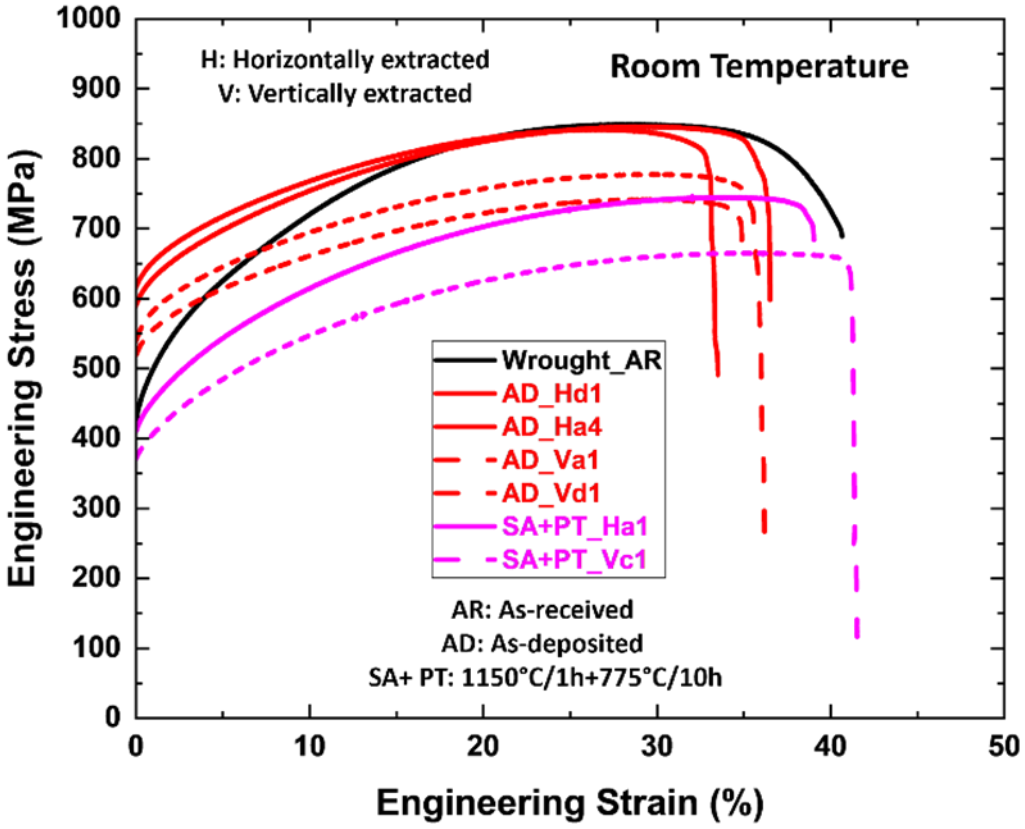

Figure 20. Engineering stress versus engineering strain plot for A709 steel fabricated via LP-DED at RT.

Table 3 provides a comprehensive comparison of the RT mechanical properties of LP-DED A709 steel across different processing conditions and the conventional wrought A709 baseline performance.

Table 3. RT tensile testing data for A709 steel fabricated via LP-DED along with wrought A709 steel in the AR condition.

Sample ID	Room Temperature		
	Yield Strength (MPa)	Ultimate Tensile Strength (MPa)	Elongation (%)
Wrought (AR)	419.67	853.47	40.65
AD_Hd1	589.09	846.33	36.51

AD_Ha4	616.15	842.05	33.51
Avg. AD Horizontal	602.62 ± 13.53	844.19 ± 2.14	35.01 ± 1.5
AD_Va1	518.81	741.89	34.96
AD_Vd1	539.66	778	36.19
Avg. AD Vertical	529.24 ± 10.43	759.95 ± 18.06	35.58 ± 0.61
SA+PT_Ha1	410.26	746.47	39.04
SA+PT_Vc1	371.20	665.93	41.52

Figure 21 presents the engineering stress–strain behavior of LP-DED A709 steel tested at 550°C, comparing AD and SA+PT heat-treated conditions at an SFR-representative temperature. Figure 21(a) shows the stress–strain curves for different specimen orientations and conditions.

Consistent with the RT results, the repeatability of the mechanical properties was observed within each specimen orientation group. However, directional anisotropy persists at elevated temperatures, as clearly illustrated by the red curves in Figure 21, representing the AD conditions. Horizontally extracted specimens (solid red lines) delivered an average YS of 437 MPa, a UTS of 661 MPa, and an elongation of 29% with excellent reproducibility between specimens (Table 4).

Vertically extracted specimens (dashed red lines) showed reduced properties, averaging a YS of 373 MPa, a UTS of 576 MPa, and an elongation of 30%. This orientation exhibited a 15% lower YS and 13% reduced UTS compared to those for the horizontal specimens, and a clear directional dependence can be observed by comparing the solid and dashed red lines in Figure 21.

The pink curves in Figure 21 show the varied response of the SA+PT specimens in both orientations. The SA+PT specimen in the horizontal orientation (pink solid line) exhibited a YS of 254 MPa, a UTS of 535 MPa, and an elongation of 36%, while the SA+PT specimen in the vertical orientation (pink dashed line) only achieved a YS of 215 MPa, a UTS of 471 MPa, and an elongation of 33%, demonstrating continued anisotropy after thermal processing with a reduction in the YS of ~42%–51% compared to that obtained for the red AD curves.

A distinctive characteristic observed for all specimens tested at 550°C was the presence of serrated flow behavior during tensile deformation, manifested as discontinuous yielding or stress oscillations in the stress–strain curves. This phenomenon can be attributed to dynamic strain aging, which results from interactions between mobile solute atoms and dislocations during deformation at elevated temperatures, consistent with the findings reported in (Mantri et al. 2025).

A benchmark comparison with the wrought AR specimen [black line in Figure 21] reveals superior DED performance: the AD specimens in the horizontal orientation achieve a 71% higher YS than the wrought AR specimens while matching the UTS, confirming the strengthening benefits of rapid solidification processing for high-temperature nuclear applications.

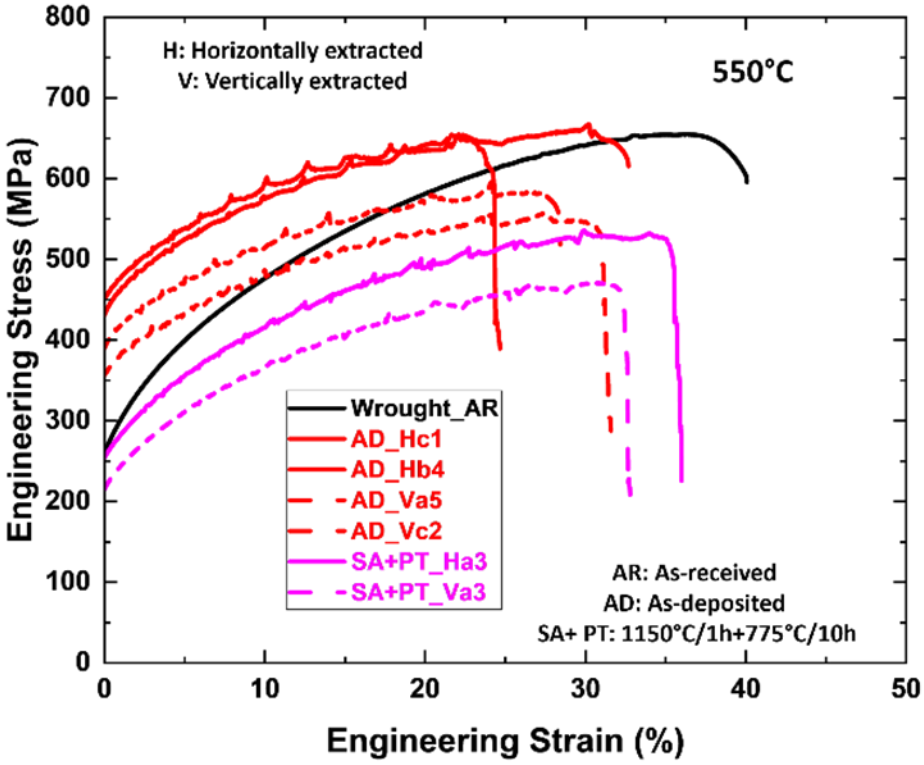

Figure 21. Engineering stress versus engineering strain plot of A709 steel fabricated via LP-DED 550°C.

Table 4 presents a comprehensive comparison of the mechanical properties measured at a reactor-relevant operating temperature (550°C) for LP-DED A709 steel across different processing conditions and the wrought A709 steel baseline performance.

Table 4. Tensile testing data measured at 550°C for A709 steel fabricated via LP-DED and wrought A709 steel in the AR condition.

Sample ID	550°C		
	Yield Strength (MPa)	Ultimate Tensile Strength (MPa)	Elongation (%)
Wrought (AR)	256.35	655.42	40.07
AD_Hc1	431.80	667.38	32.68
AD_Hb4	442.81	654.53	24.66
Avg. AD Horizontal	437.31 ± 5.51	660.96 ± 6.43	28.67 ± 4.01
AD_Va5	356.18	557.56	31.59
AD_Vc2	390.01	595.83	28.43
Avg. AD Vertical	373.10 ± 16.92	576.70 ± 19.14	30.01 ± 1.58
SA+PT_Ha3	254.42	535.70	35.99
SA+PT_Va3	214.82	470.74	32.81

Temperature-dependent mechanical behavior is clearly illustrated through comparative plots, demonstrating how the elevated temperature significantly affects the stress–strain characteristics of DED A709 steel. The RT curves in Figure 22(a) exhibit higher strength levels

and smoother plastic flow behavior, while the 550°C curves in Figure 22(b) show reduced strength but enhanced ductility with characteristic serrated flow patterns.

The representative nature of these plots allows for a direct assessment of temperature-dependent performance degradation, critical for nuclear reactor applications where components must maintain structural integrity across varying thermal conditions. Figure 22 serves as a comprehensive reference for understanding the fundamental mechanical behavior changes that occur in DED A709 steel when transitioning from ambient to SFR operating temperatures.

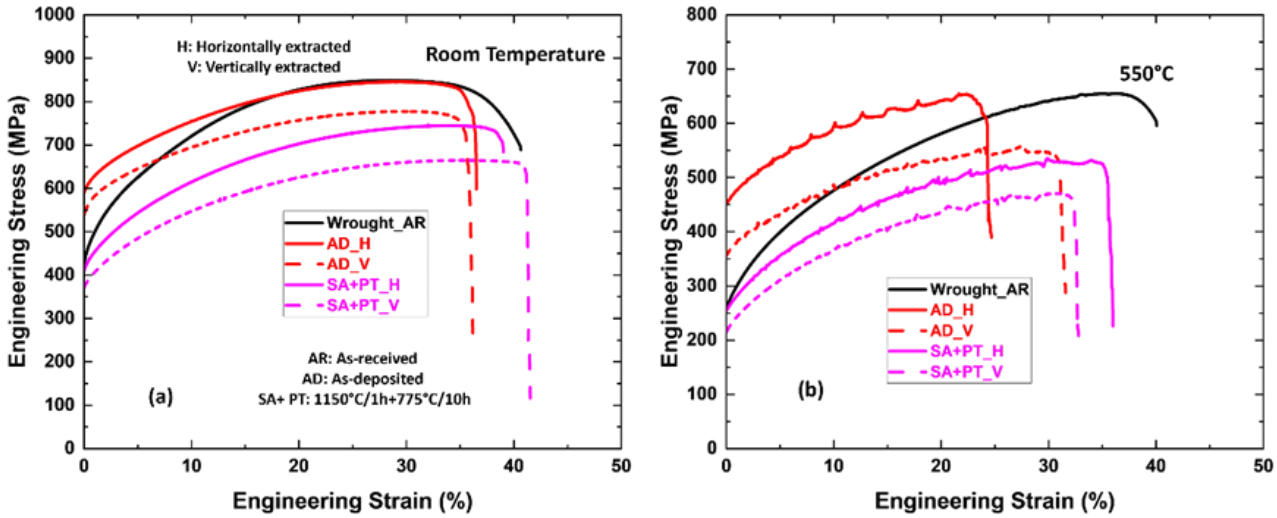

Figure 22. Representative engineering stress versus engineering strain plot of A709 steel fabricated via LP-DED at (a) RT and (b) 550°C.

4.3 Fractography

Figure 23 presents a low magnification fractographic analysis of the fracture surfaces from both AD LP-DED and wrought AR A709 steel specimens tested at RT and 550°C. The comparative fractographic examination reveals distinct differences in the fracture characteristics and void formation behavior between the two processing conditions.

The fracture surface of the RT AD specimen exhibited a heterogeneous void population consisting of both large pores and fine microvoids [Figure 23(b)]. The presence of large pores in the AM condition can be attributed to processing-related defects such as incomplete powder melting, gas entrapment, or lack-of-fusion defects characteristic of the DED process. These larger defects serve as stress concentration sites and potential crack initiation locations during tensile loading.

In contrast, the RT wrought AR specimen displayed a more uniform fracture morphology predominantly characterized by fine microvoid formation. The absence of large processing-related pores in the wrought material reflects the superior consolidation achieved through conventional thermomechanical processing routes, resulting in a more homogeneous microstructure with fewer defect sites.

Additional fractographic analysis of the wrought RT specimens revealed that fracture propagation occurred primarily along grain boundaries (Figure 23a), indicating intergranular failure mechanisms consistent with the findings reported in (Mantri et al. 2025). This

intergranular fracture mode in the wrought condition suggests that grain boundary cohesion represents the controlling factor for fracture resistance, whereas the AM condition exhibits more complex fracture behavior influenced by both microstructural features and processing-induced defects.

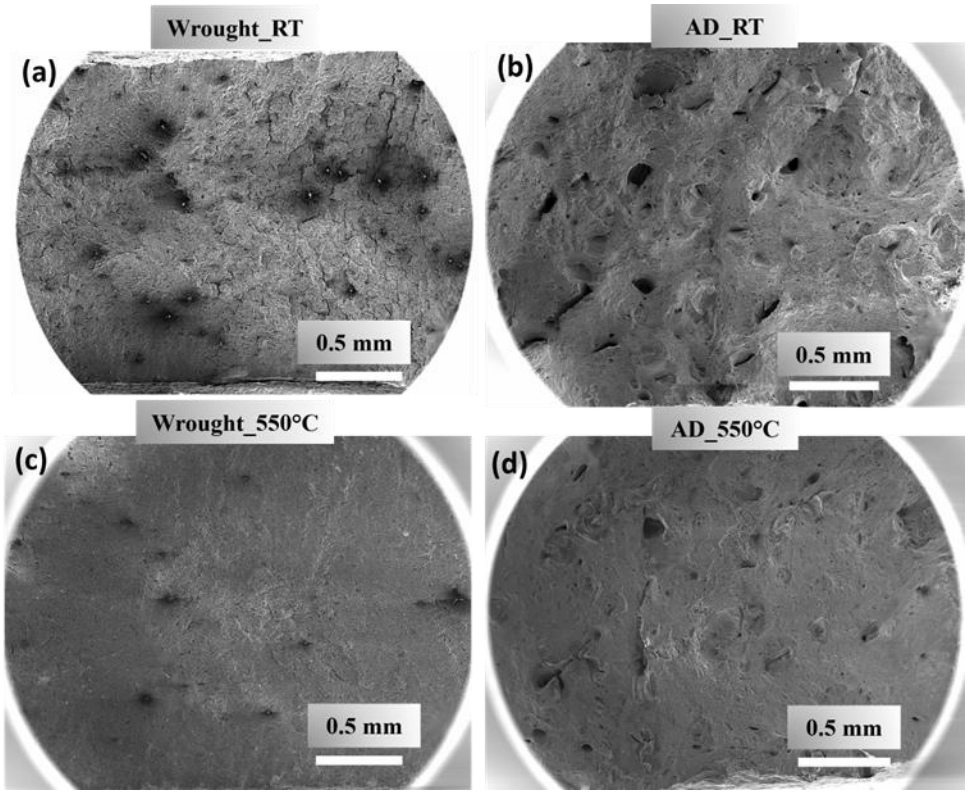

Figure 23. Representative RT and 550°C fracture surfaces of AD and wrought AR A709 steel at low magnification.

The higher magnification fractographic examination presented in Figure 24 provides detailed insight into the fracture mechanisms operative in both the wrought AR and AD DED A709 steel specimens. The fracture surfaces for both material conditions revealed the characteristic dimpled morphology associated with ductile fracture, indicating that failure occurred through microvoid nucleation, growth, and coalescence processes despite the differences in processing routes and initial microstructural features.

The presence of dimples on the fracture surfaces confirms that both wrought and AM conditions maintain sufficient ductility for energy-absorbing failure mechanisms, which are critical for nuclear structural applications where catastrophic brittle failure must be avoided. The dimple formation process involves the nucleation of voids at second-phase particles, inclusions, or microstructural discontinuities, followed by plastic-deformation-driven void growth and eventual coalescence to create the characteristic cup-and-cone fracture topology. This ductile failure mode indicates that the material retains adequate toughness despite the elevated strength levels achieved through AM processing.

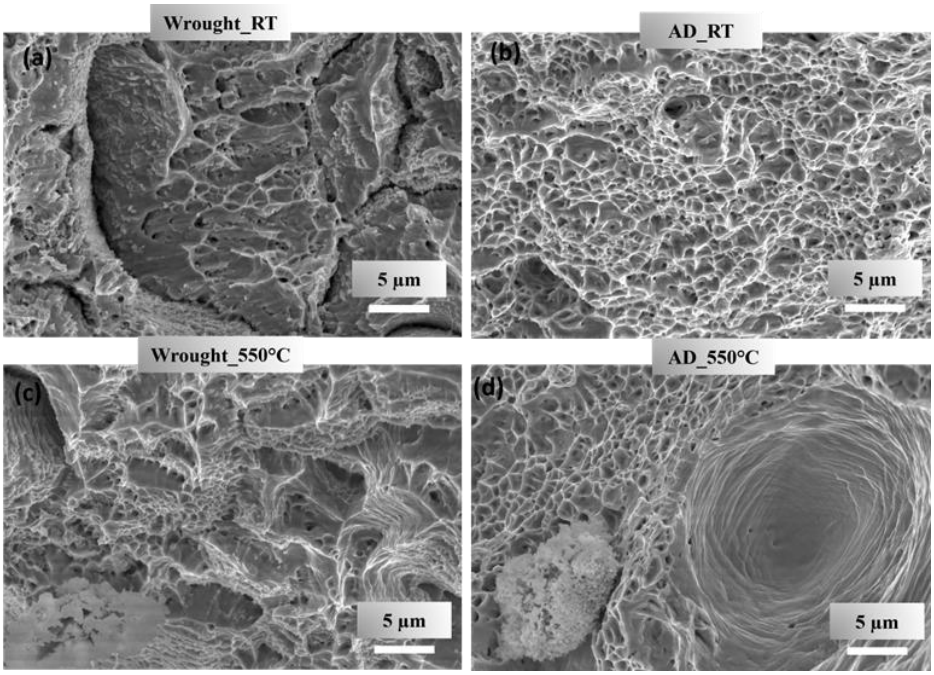

Figure 24. Representative RT and 550°C fracture surfaces of AD and wrought AR A709 steel at higher magnification.

5.0 Ion Irradiation

Figure 25 presents the depth-dependent profiles of displacements per atom and injected interstitials calculated using the Stopping and Range of Ions in Matter (SRIM) Monte Carlo simulation code. SRIM modeling provides a theoretical framework for understanding the spatial distribution of radiation damage by simulating how energetic ions interact with the target material as they penetrate and deposit energy through the sample thickness.

The computational results demonstrate that both the displacements per atom and injected interstitials profiles reach their maximum value at approximately 1 μm below the sample surface. This depth corresponds to the region of maximum energy deposition, where incoming ions lose the greatest amount of energy through nuclear collisions with target atoms before coming to rest. The displacements per atom profile represents the cumulative displacement damage caused by primary knock-on atoms and subsequent collision cascades that create vacancies and interstitials throughout the damaged region. The injected interstitials profile indicates the spatial distribution of excess atoms forced into non-lattice positions during the irradiation process, contributing to local lattice distortion and microstructural evolution.

The significance of these depth-dependent damage distributions is that the maximum void swelling and microstructural changes are expected to occur at approximately 1 μm from the sample surface, where the concentration of radiation-induced defects is highest. This understanding is critical for interpreting post-irradiation microstructural characterization results, as the most significant radiation effects will be concentrated in this near-surface region rather than being uniformly distributed throughout the sample thickness.

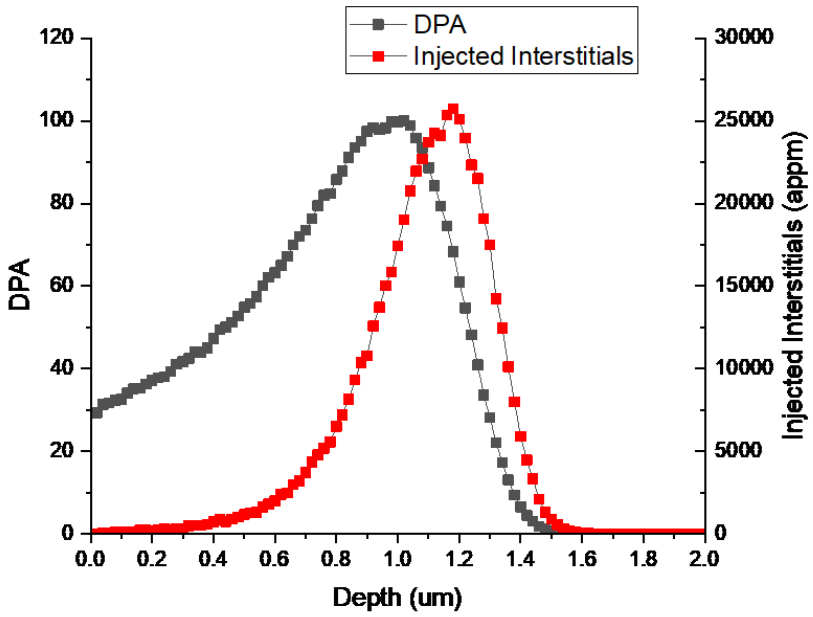

Figure 25. Displacements per atom and injected interstitials profiles as a function of depth.

HAADF-STEM imaging of AD DED A709 steel following 100 dpa ion irradiation provides critical insight into the radiation-induced microstructural evolution and damage mechanisms in AM austenitic stainless steel. The overview image in Figure 26(a) confirms the depth-dependent

damage distribution predicted by SRIM calculations, with the most severe radiation damage concentrated within the top 1 μm region as evidenced by exceptionally high dislocation densities and the formation of radiation-induced voids. The higher magnification image in Figure 26(b) reveals the detailed nature of the radiation-induced dislocation networks and void sizes, demonstrating the complex defect structures that develop under high-energy ion bombardment and contribute to material property degradation through mechanisms such as radiation hardening and void swelling (Zhang et al. 2021; Kim et al. 2019). Most significantly, the complementary XEDS elemental maps in Figure 26(c) reveal pronounced radiation-induced segregation effects, with strong Ni enrichment occurring in specific regions while Cr and Fe segregate to other areas within the irradiated zone (Liu 2018). This elemental redistribution represents a critical degradation mechanism in austenitic stainless steels under irradiation, as the depletion of Cr from certain regions can compromise corrosion resistance while Ni segregation can alter local mechanical properties and phase stability. The observed segregation behavior is particularly important for nuclear applications, as it can lead to the formation of brittle phases, reduced grain boundary cohesion, and accelerated corrosion in reactor coolant environments, ultimately affecting the long-term structural integrity of AM components in nuclear reactors.

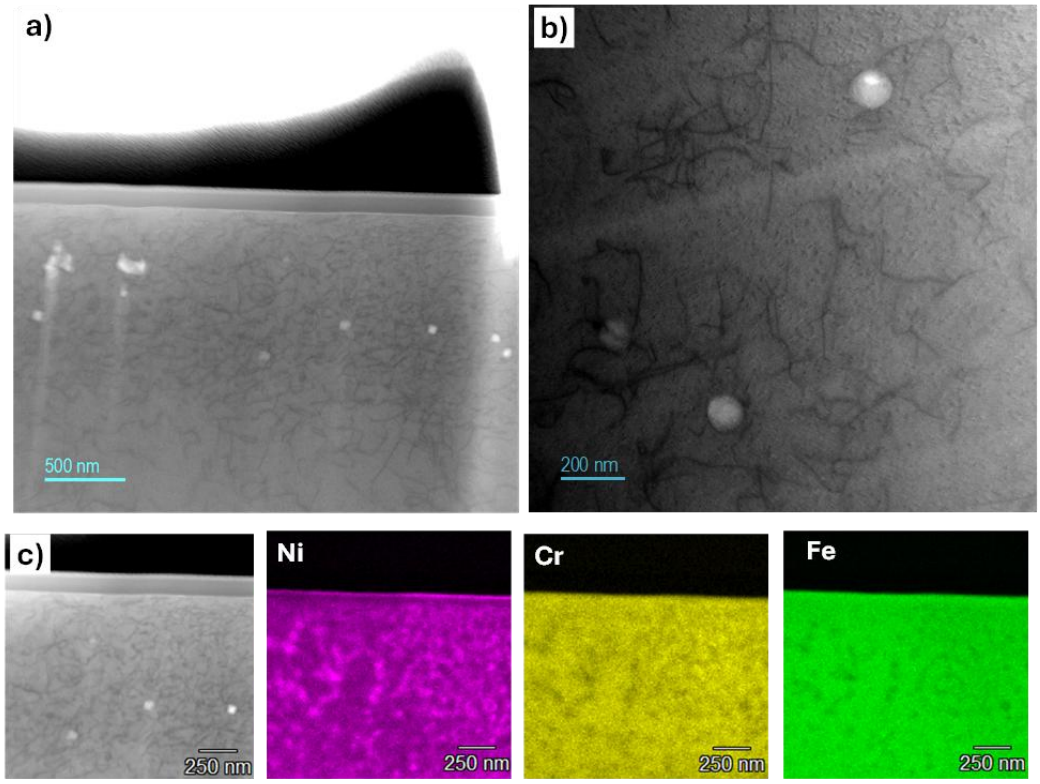

Figure 26. HAADF-STEM characterization of DED A709 steel subjected to 100 dpa ion irradiation. (a) Overview showing the extent of damage characterized by a high dislocation density in the top 1 μm region along with voids. (b) Higher magnification image revealing the nature of the dislocations and void sizes. (c) XEDS elemental maps showing strong Ni segregation after ion irradiation and Cr and Fe segregation to other regions.

An examination AD DED A709 steel following 200 dpa ion irradiation reveals escalated damage progression with a marked increase in the void density within the damage region, as shown in

Figure 27(a). This indicates accelerated void nucleation and growth processes that directly contribute to volumetric swelling and the deterioration of mechanical properties. The persistent segregation patterns in Figure 27(b) demonstrate that the elemental redistribution intensifies rather than saturates, with sustained Ni enrichment and Cr/Fe depletion suggesting ongoing compositional instability that may establish more severe chemical gradients. This dose-dependent evolution provides essential insight into degradation kinetics, indicating that radiation-induced segregation is a progressive process that continues evolving with extended exposure, potentially leading to increasingly compromised local properties and phase stability that are critical for the longevity of nuclear reactor components.

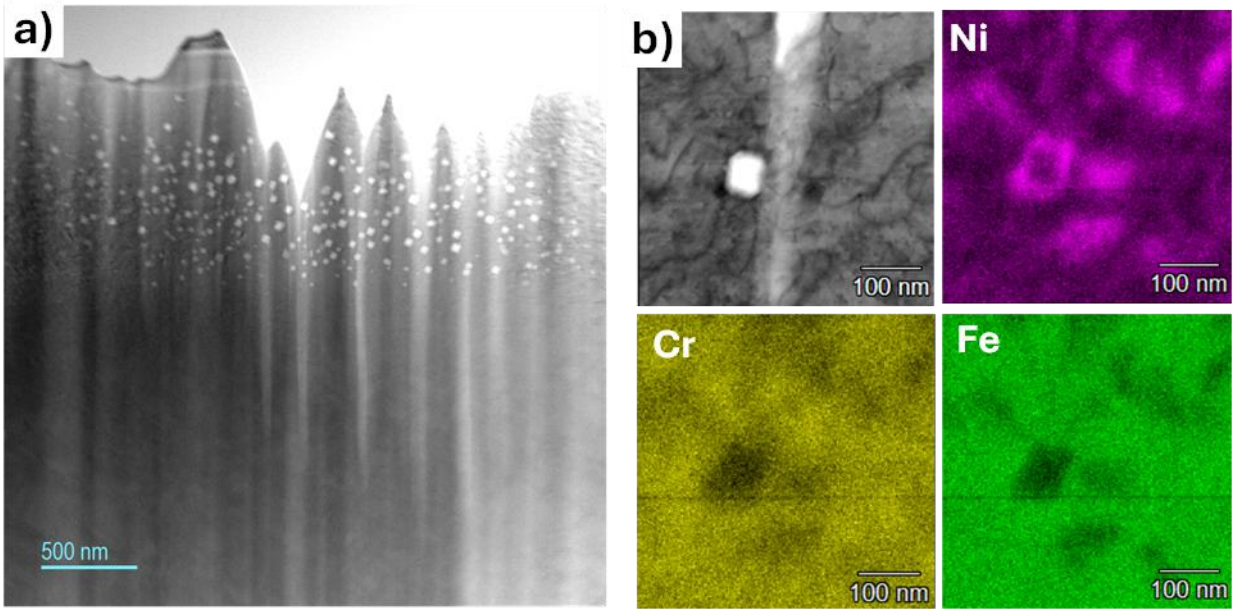

Figure 27. HAADF-STEM characterization of DED A709 steel subjected to 200 dpa ion irradiation. (a) Overview showing the extent of damage characterized by a high void density in the top 1 μm region. (b) Higher magnification image revealing the nature of the dislocations and void sizes and XEDS elemental maps showing strong Ni segregation after ion irradiation and Cr and Fe segregation to other regions.

The 300 dpa condition shows continued damage progression with further void density increases in Figure 28(a). The sustained segregation effects in Figure 28(b) confirm the ongoing nature of degradation processes in additively manufactured A709 steel.

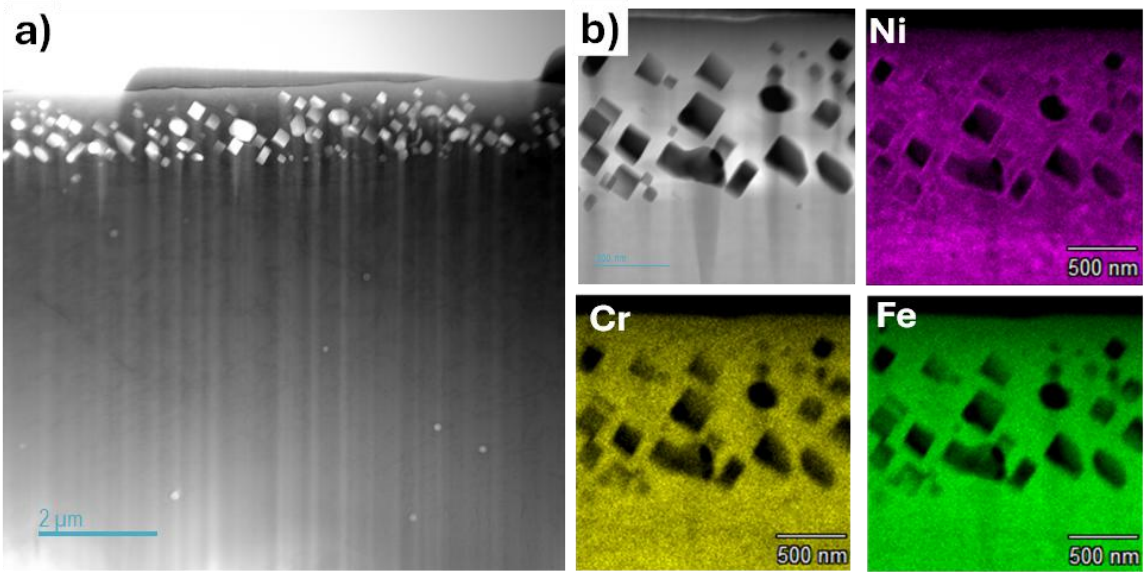

Figure 28. HAADF-STEM characterization of DED A709 steel subjected to 300 dpa ion irradiation. (a) Overview showing the extent of damage characterized by a high void density in the top 1 µm region. (b) Higher magnification image revealing the nature of the dislocations and void sizes and XEDS elemental maps showing strong Ni segregation after ion irradiation and Cr and Fe segregation to other regions.

At the maximum 400 dpa dose, the most extensive radiation damage is observed in Figure 29(a), showing a peak void density concentration. The elemental maps in Figure 29(b) show the most pronounced radiation-induced segregation effects, with substantial Ni accumulation and the corresponding Cr/Fe redistribution, establishing the ultimate degradation state for additively manufactured A709 steel under current ion irradiation conditions.

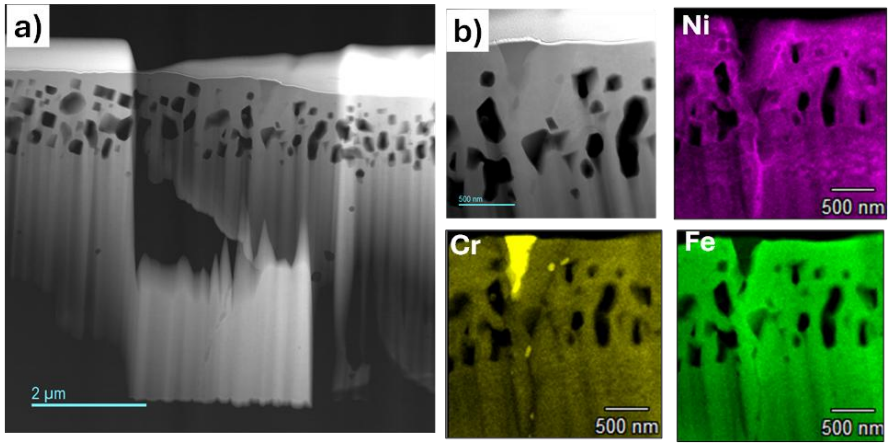

Figure 29. HAADF-STEM characterization of DED A709 steel subjected to 400 dpa ion irradiation. (a) Overview showing the extent of damage characterized by a high void density in the top 1 µm region. (b) Higher magnification image revealing the nature of the dislocations and void sizes and XEDS elemental maps showing strong Ni segregation after ion irradiation and Cr and Fe segregation to other regions.

6.0 G-92 Results and Discussion

To understand the high-temperature behavior of additively manufactured G-92 steel, specimens were subjected to systematic heat treatment protocols designed to achieve the desired tempered martensitic microstructure with controlled carbide precipitation that are essential for nuclear applications. Characterization using electron microscopy and tensile testing established microstructure–property relationships at ambient and reactor operating temperatures (550°C).

6.1 Microstructure Analysis

A comprehensive analysis of G-92 steel was conducted under different heat treatment conditions, including AD, normalizing, tempering, and combined normalizing–tempering processing.

6.1.1 As-Deposited

Microstructural characterization of AD DED G-92 steel through complementary backscattered electron SEM and HAADF-STEM imaging reveals the complex multiphase microstructural characteristics of F/M steels subjected to rapid solidification during DED processing. The overall microstructure in Figure 30(a, c) shows the coexistence of ferrite and martensite phases in the AD condition, reflecting the nonequilibrium cooling rates experienced during the DED process that result in incomplete martensitic transformation. High magnification images [Figure 30(b, d)] reveal the presence of fine needle-shaped precipitates distributed throughout the matrix, most likely θ-phase (Fe_3C) carbides in the ferrite phase that formed during the thermal cycling inherent to layer-by-layer deposition (Eftink et al. 2021).

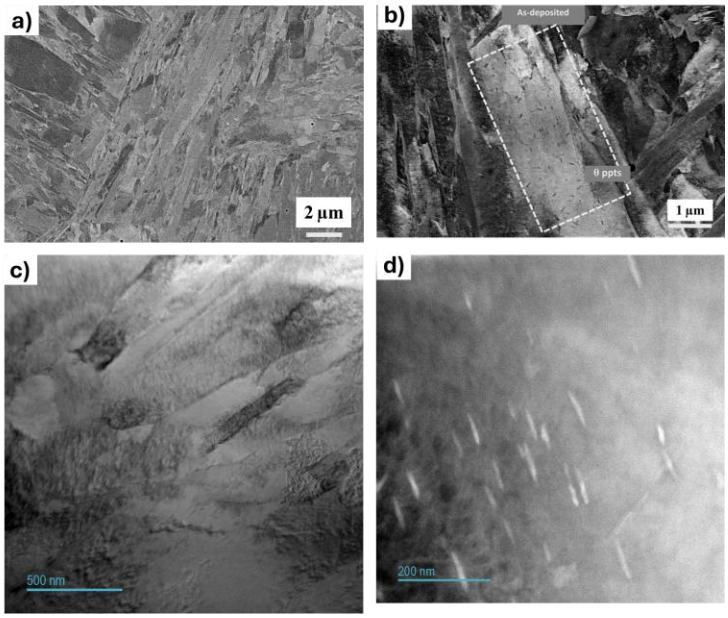

Figure 30. Microstructural characterization of AD DED G-92 steel. (a–b) Backscattered electron SEM images at different magnifications and (c–d) the corresponding HAADF-STEM images. (a, c) Overall microstructure showing ferrite and martensite in the AD condition. (b, d) High magnification images revealing needle-shaped precipitates, most likely the θ phase.

The EBSD IPF+IQ map in 31(a) provides detailed crystallographic information showing the characteristic lath martensite distribution and sizes, which are critical for understanding the strength and toughness balance in the AD condition. The KAM and GND density maps of G-92 steel were calculated from high-resolution EBSD data acquired over an area of approximately 80 × 80 μm, with an indexing rate exceeding 90% and a step size of 50 nm, as presented in Figure 30(b). These data enabled accurate quantification of the local crystallographic misorientation and dislocation density variations across the microstructural features. GNDs were found to be heterogeneously distributed throughout the microstructure, reflecting the complex deformation history and thermal processing effects inherent to the DED process. This heterogeneous distribution pattern indicates localized strain accumulation zones associated with rapid solidification, thermal cycling, and microstructural boundaries where dislocation networks preferentially develop during processing. The average GND density was measured to be $17.04\times10^{14}/m^2$, representing the elevated dislocation content characteristic of rapid solidification and thermal cycling during layer-by-layer deposition. The grain reference orientation deviation (GROD) map in Figure 31(c) illustrates the intragranular misorientation distribution, highlighting areas of local lattice distortion and residual strain accumulation within individual grains. The PF and IPF in Figure 31(d-e) demonstrate the crystallographic texture and preferred orientation relationships within the steel, revealing that no significant texture was developed in the AD condition. This high dislocation density significantly contributes to the exceptional strength observed in AD DED G-92 steel through dislocation strengthening mechanisms.

This comprehensive microstructural analysis establishes the baseline condition for subsequent heat treatment optimization, highlighting the need for controlled thermal processing to achieve the desired tempered martensitic microstructure with optimized carbide precipitation that is essential for high-temperature nuclear applications.

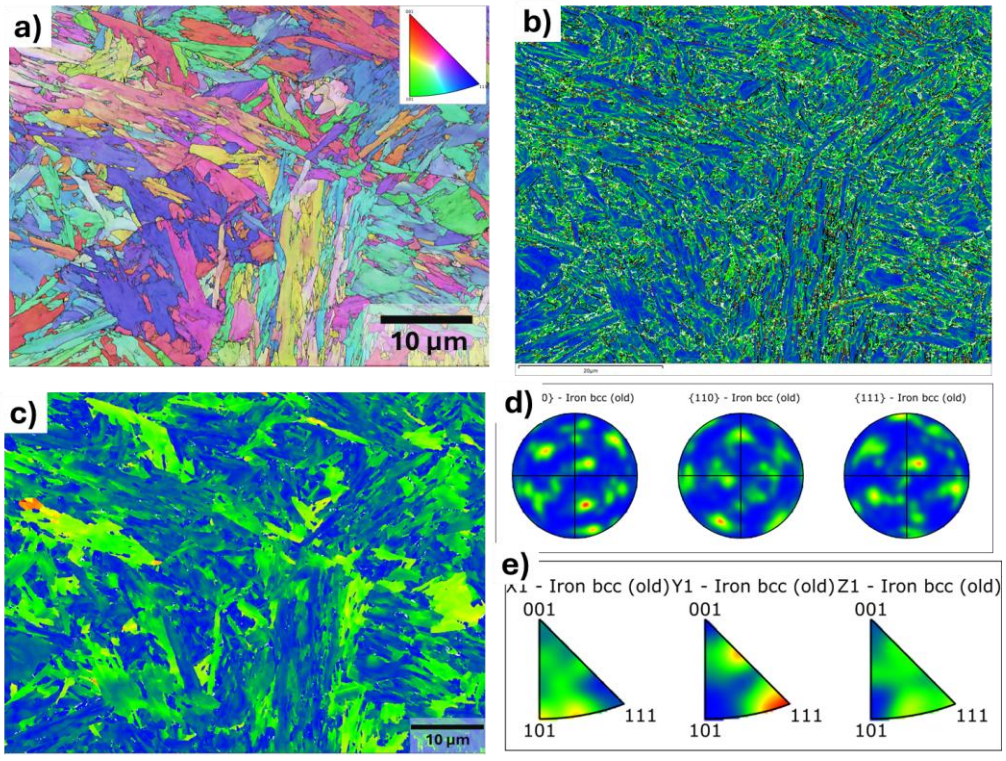

Figure 31. Orientation microscopy of AD DED G-92 steel. (a) IPF map revealing lath martensite morphology and grain sizes, (b) KAM map, (c) GROD map, (d) pole figures, and (e) inverse pole figures.

6.1.2 Normalizing Treatment

Microstructural characterization of DED G-92 steel following a normalizing heat treatment demonstrates its effectiveness in achieving a more homogeneous microstructural condition compared to that of the AD state. The backscattered electron SEM image in Figure 32(a) and complementary HAADF-STEM images in Figures 32(b–c) reveal a notable absence of precipitates throughout the matrix, confirming that the normalizing temperature was sufficient to dissolve the needle-shaped θ-phase carbides observed in the AD condition and create a supersaturated solid solution. This precipitate-free condition indicates successful austenitization during the normalizing treatment, followed by air cooling that produced fresh martensite without time for significant carbide precipitation.

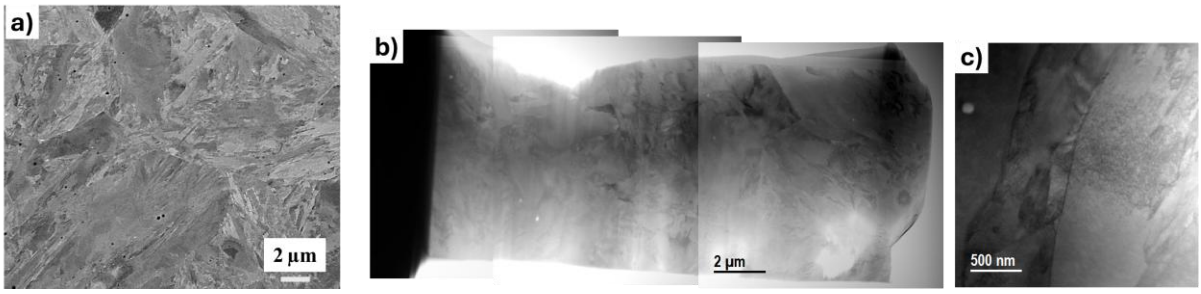

Figure 32. Microstructural characterization of DED G-92 steel after a normalizing heat treatment. (a) Backscattered electron SEM image and (b–c) HAADF-STEM images showing the lack of precipitates in the matrix.

The IPF+IQ map in Figure 30(a) shows the refined lath martensite distribution and sizes resulting from the controlled thermal transformation, with the martensitic laths exhibiting a more uniform morphology compared to that of the mixed F/M structure present in the AD condition. The corresponding KAM map in Figure 32(b) reveals the strain distribution within the normalized microstructure. Notably, the normalizing treatment alone resulted in the highest average GND density, measured at $20.23\times10^{14}/m^2$, representing an 18% increase over that for the AD condition. This counterintuitive increase can be attributed to the rapid cooling from the high temperature that promotes a martensitic transformation with enhanced dislocation generation, potentially creating a more heavily dislocated martensitic structure than that of the AD condition.

This normalized microstructural state represents an intermediate processing step that provides a clean starting point for subsequent tempering treatments designed to precipitate fine, uniformly distributed carbides essential for optimizing the high-temperature mechanical properties. The GROD map in Figure 30(c) reveals the reduced intragranular strain patterns compared to the as-deposited condition. The pole figures Figure 30(d) and inverse pole figures Figure 30(e) demonstrate a slightly modified texture and crystallographic orientation. This analysis provides essential information about how normalizing treatment alters the microstructural state and crystallographic properties of the additively manufactured steel, affecting its mechanical performance and structural integrity.

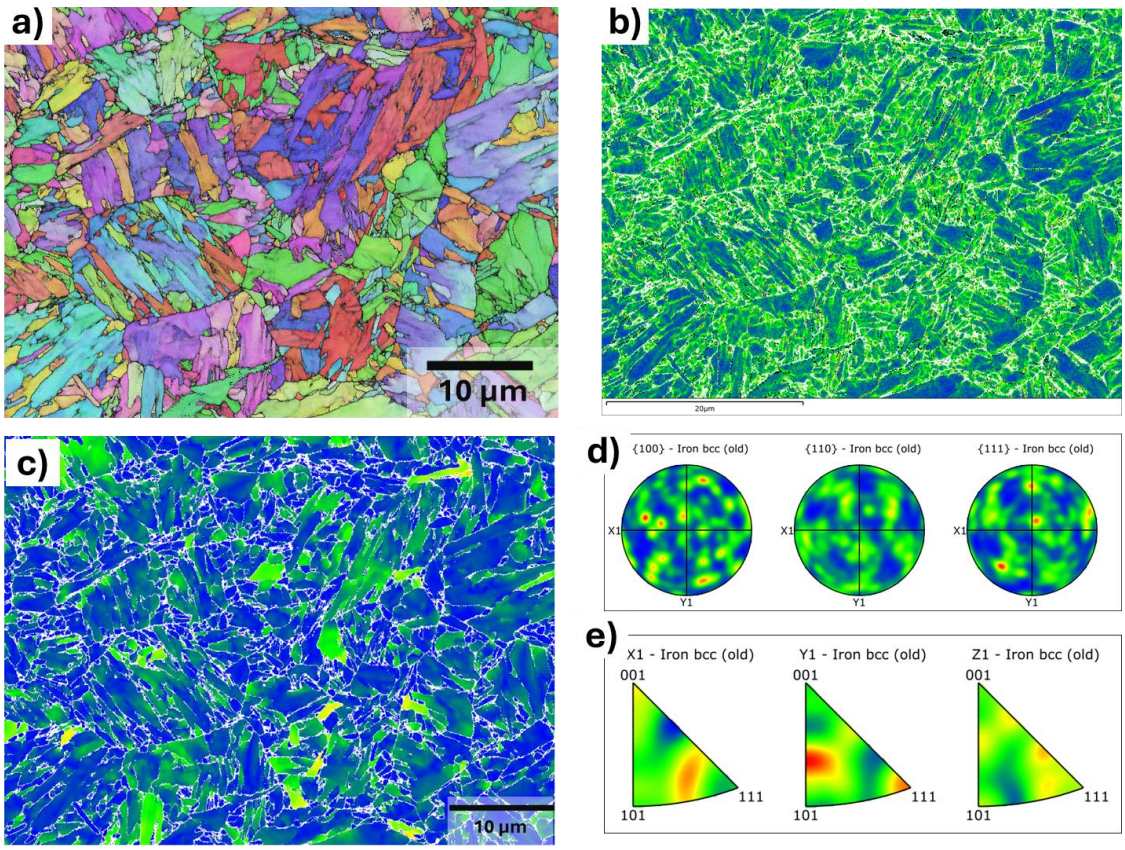

Figure 33. Orientation microscopy of DED G-92 steel after normalizing treatment. (a) IPF map revealing lath martensite morphology and grain sizes, (b) KAM map, (c) GROD map, (d) pole figures, and (e) inverse pole figures.

6.1.3 Tempering Treatment

Advanced microstructural characterization of DED G-92 steel demonstrates the specific thermal modifications achieved through a tempering treatment (775°C/45 minutes) designed to develop optimal mechanical properties for nuclear reactor applications. Figure 34(a) shows the backscattered electron SEM analysis revealing the evolved tempered martensitic structure, where controlled thermal aging has transformed the fresh martensite into a refined microstructure characterized by fine carbide precipitation. The tempering-induced changes are evident through the modified contrast patterns that indicate carbide formation and partial structural recovery from the initial martensitic condition.

Figure 34(b) shows the IPF+IQ map that confirms the preservation of the characteristic lath martensitic morphology during thermal exposure. The crystallographic orientation analysis demonstrates that the fundamental martensitic structure remains intact. Figure 34(c) shows the KAM analysis, which provides critical quantitative insight into the strain state and dislocation distribution after tempering. The measured average GND density of approximately $17.0\times10^{14}/m^2$ remarkably matches that for the AD condition, revealing that the applied tempering parameters were thermally insufficient to activate significant dislocation recovery mechanisms. This implies that the tempering treatment operated primarily through carbide precipitation pathways rather

than dislocation annihilation processes. This selective microstructural modification preserves the high dislocation density responsible for strength retention while enabling carbide formation that improves the toughness characteristics. The GROD map in Figure 34(d) displays intragranular misorientation patterns and local strain distributions within the microstructure.

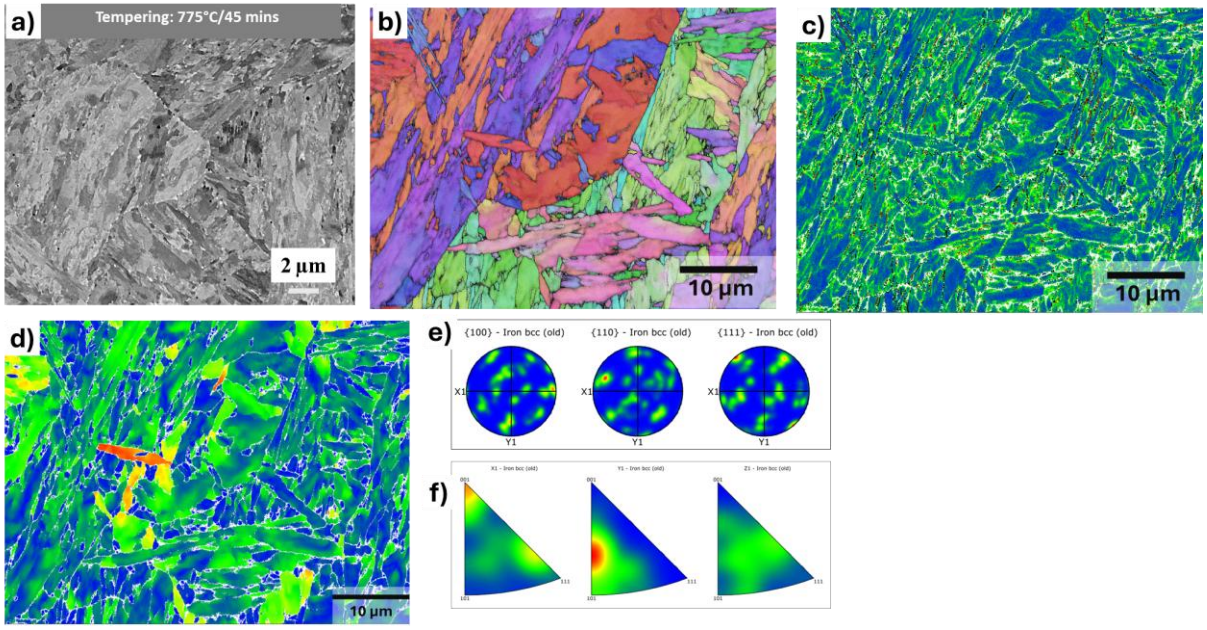

Figure 34. Microstructural characterization of DED G-92 steel after the tempering heat treatment. (a) Backscattered electron SEM image, (b) IPF map revealing lath martensite morphology and grain sizes, (c) KAM map, (d) GROD map, (e) pole figures, and (f) inverse pole figures.

Figure 35 shows SEM-XEDS maps of DED G-92 steel following the tempering heat treatment that provide critical insight into the elemental distribution and precipitation chemistry that develop during the controlled thermal aging process. The analysis reveals the partitioning behavior of key alloying elements, including Cr, manganese (Mn), and W, between the tempered martensitic matrix and the $M_{23}C_6$ carbide precipitates at the grain boundaries. This elemental analysis is crucial for validating that the heat treatment has successfully developed the desired precipitation chemistry required for nuclear reactor applications, where precise control of the carbide composition and distribution directly influences the long-term stability of the mechanical properties and the creep resistance under elevated temperature service conditions.

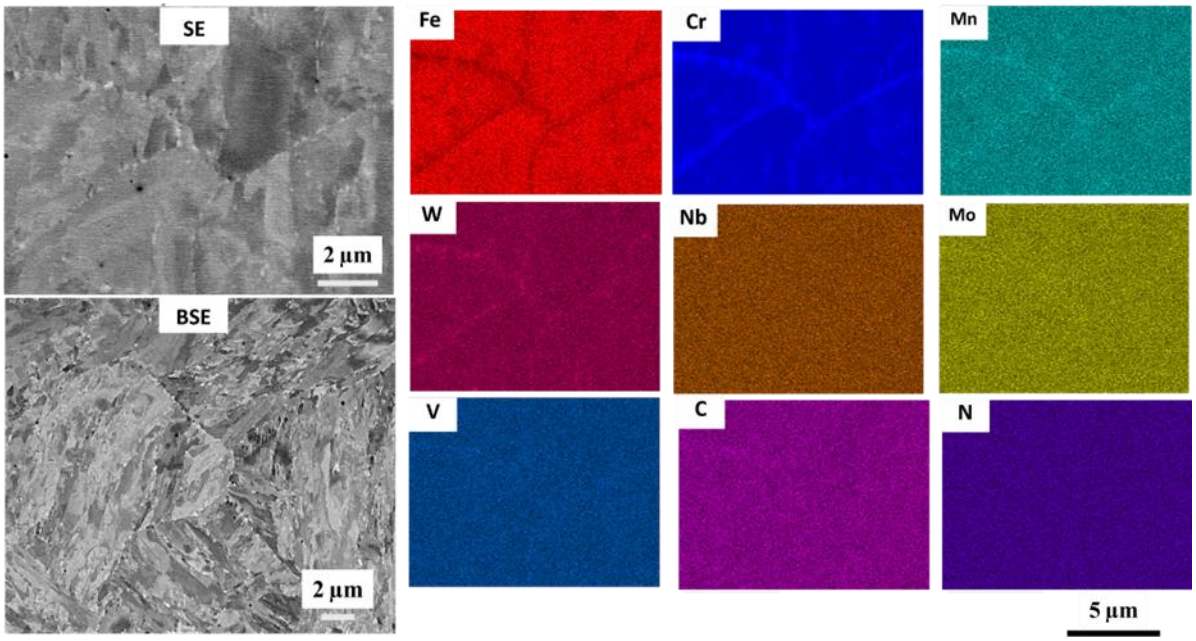

Figure 35. XEDS maps of DED G-92 steel after tempering.

STEM characterization of DED G-92 steel following the tempering heat treatment reveals the successful development of a complex precipitation microstructure essential for high-temperature mechanical performance in F/M steels. The HAADF-STEM images in Figures 36(a–d) show the formation of two distinct precipitate populations: coarser precipitates located at the grain boundaries and finer nanoscale precipitates distributed within the grains, representing the characteristic precipitation hierarchy that develops during the controlled tempering of G-92 steel. The grain boundary precipitates likely consist of $M_{23}C_6$ carbides enriched in Cr and Mo that provide grain boundary strengthening and contribute to the creep resistance by impeding grain boundary sliding at elevated temperatures. The intragranular nanoscale precipitates are expected to be MX-type carbonitrides rich in V and Nb that provide effective dislocation pinning and precipitation strengthening through coherency strains and Orowan strengthening mechanisms. This dual precipitation structure is critical for achieving the superior high-temperature properties of G-92 steel, as the combination of grain boundary strengthening and matrix precipitation hardening provides enhanced creep resistance and thermal stability compared to those of conventional F/M steels.

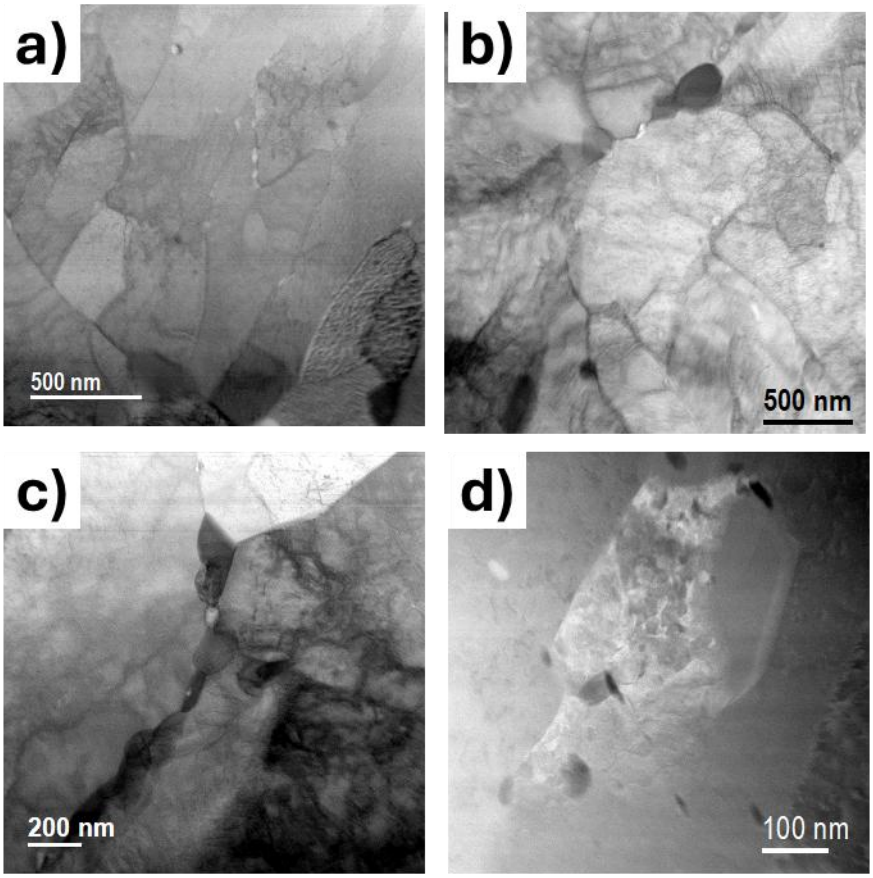

Figure 36. HAADF-STEM characterization of DED G-92 steel after a tempering heat treatment. (a–d) Images revealing the presence of precipitates at the grain boundaries and nanoscale precipitates within the grains.

Figure 37 shows an STEM-XEDS analysis of a DED G-92 steel specimen following the tempering heat treatment. This analysis provides detailed compositional characterization of the nanoscale MX precipitates that significantly contribute to the steel's high-temperature strengthening mechanisms. Figure 37(a) reveals the fine-scale precipitate distribution achieved through controlled tempering, while the corresponding chemical maps in Figure 37(b) show that these MX precipitates are enriched in V, N, S, which is expected for the beneficial VN or V(C, N) carbonitride phases that provide effective precipitation strengthening. However, the elemental maps also reveal unexpected enrichment of Mn and S within these precipitates (apart from the $M_{23}C_6$ grain/lath boundaries precipitates), indicating a more complex precipitation chemistry.

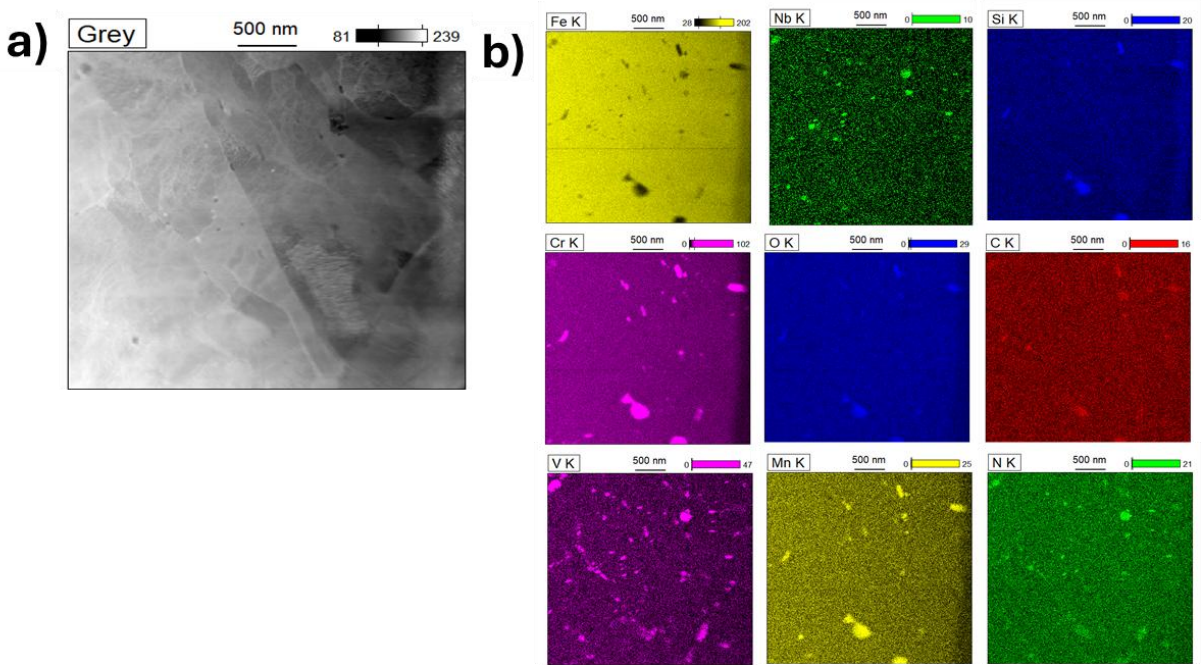

Figure 37. STEM-XEDS maps of DED G-92 steel after the tempering heat treatment. (a) HAADF-STEM image and (b) the corresponding chemical maps of the matrix showing MX precipitates enriched in V, N, Mn, and S.

6.1.4 Normalizing + Tempering Condition

Advanced characterization of DED G-92 steel demonstrates how the sequential normalizing–tempering heat treatment achieves superior microstructural optimization through systematic thermal processing designed specifically for F/M steel applications.

The two-step thermal processing sequence successfully transforms the AD mixed microstructure through distinct mechanisms: the initial normalizing stage completely austenitizes the material, eliminating heterogeneous F/M phases, while the subsequent air cooling produces fresh martensite that serves as an optimal starting point for controlled tempering-induced modifications.

Figure 38(a) reveals the refined tempered martensitic architecture achieved through this systematic approach, where backscattered electron SEM imaging captures the homogeneous microstructural development resulting from complete phase transformation followed by controlled carbide precipitation and matrix modification during tempering.

Figure 38(b) demonstrates the benefits of this sequential processing through an IPF+IQ analysis by showing characteristic lath martensitic distributions with refined grain dimensions and enhanced morphological consistency compared to single-step treatments. This uniformity confirms that the normalizing stage effectively homogenized the microstructure prior to the tempering-induced precipitation events.

Figure 38(c) quantifies the optimized strain characteristics through a KAM map, revealing substantially reduced residual stress distributions and improved microstructural stability. A quantitative dislocation analysis shows remarkable microstructural improvement, with a significantly decreased GND density of $11.01\times10^{14}/m^2$—a 35% reduction from that in the AD

state. This substantial improvement results from the synergistic effects of the normalizing-induced microstructural reset combined with the tempering-enabled recovery processes that promote dislocation polygonization and stable arrangement formation. The GROD map in Figure 38(d) demonstrates the intragranular misorientation and residual strain compared to single-step treatments.

From a processing mechanism viewpoint, austenitization fundamentally resets the dislocation network, while the subsequently controlled cooling and tempering activate recovery mechanisms that optimize both the strength and ductility through a balanced dislocation density reduction and the development of carbide precipitation.

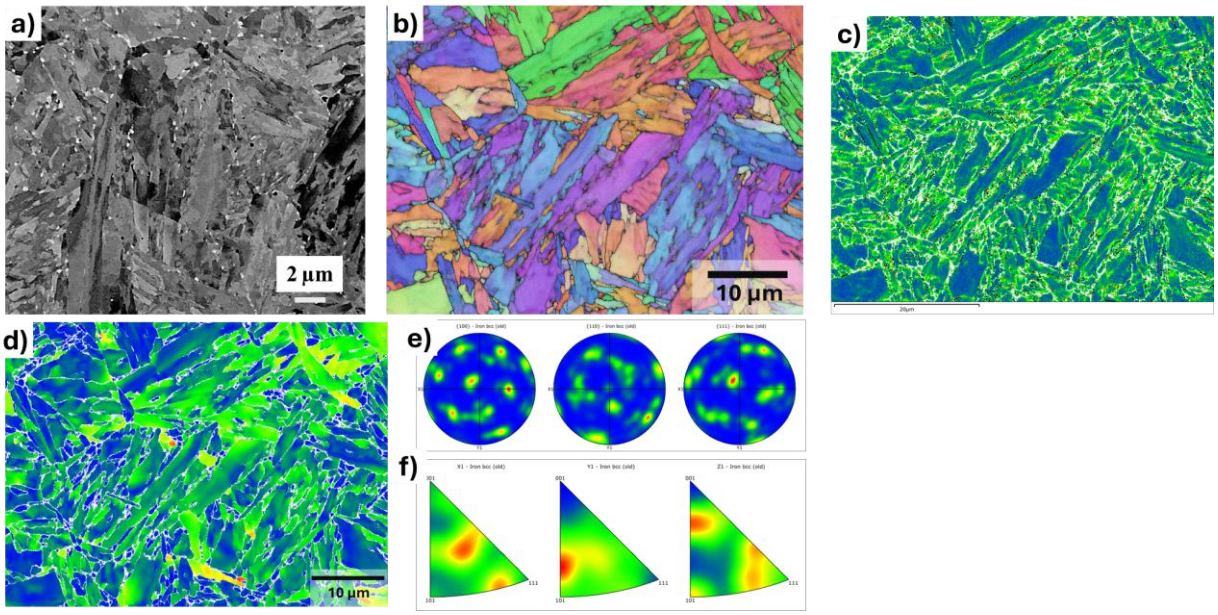

Figure 38. Microstructural characterization of DED G-92 steel after the normalizing + tempering heat treatment. (a) Backscattered electron SEM image. (b) IPF map revealing lath martensite morphology and grain sizes, (c) KAM map, (d) GROD map, (e) pole figures, and (f) inverse pole figures.

HAADF-STEM analysis reveals the optimized precipitation architecture in DED G-92 steel following the sequential normalizing–tempering treatment. Figures 39(a–d) show the successful development of dual precipitate populations: grain boundary $M_{23}C_6$ precipitates and fine nanoscale MX precipitates uniformly distributed within grains. This demonstrates that normalizing created homogeneous starting conditions for controlled precipitation during tempering. The advantage of this sequential processing is that normalizing functions as a microstructural reset, eliminating prior heterogeneities and creating uniform martensite that serves as an optimal foundation for controlled carbide precipitation during subsequent tempering. This results in a superior precipitate distribution compared to that obtained from the direct tempering of AD material, providing balanced strengthening for nuclear applications.

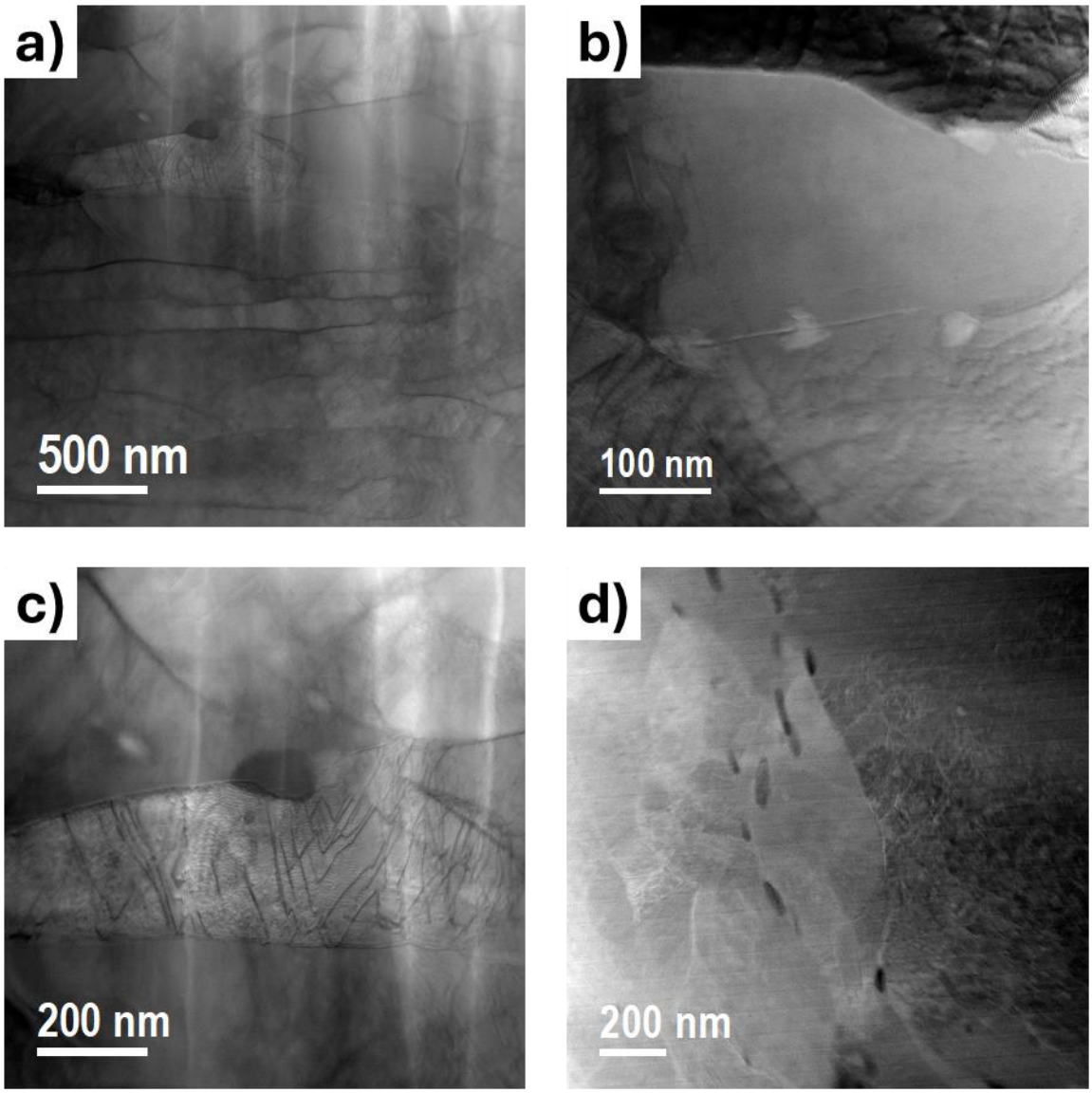

Figure 39. HAADF-STEM characterization of DED G-92 steel after the normalizing + tempering heat treatment. (a–d) Images revealing the presence of precipitates at the grain boundaries and nanoscale precipitates within the grains.

An STEM-XEDS analysis of G-92 steel following the normalizing–tempering treatment reveals strategic dual precipitation: (V, Nb)N at the martensitic lath boundaries and tungsten-enriched $M_{23}C_6$ carbides at the grain boundaries, as shown in Figure 40. This dual precipitation system delivers the enhanced creep resistance and thermal stability required for G-92 nuclear reactor components through both lath boundary strengthening and matrix precipitation hardening mechanisms.

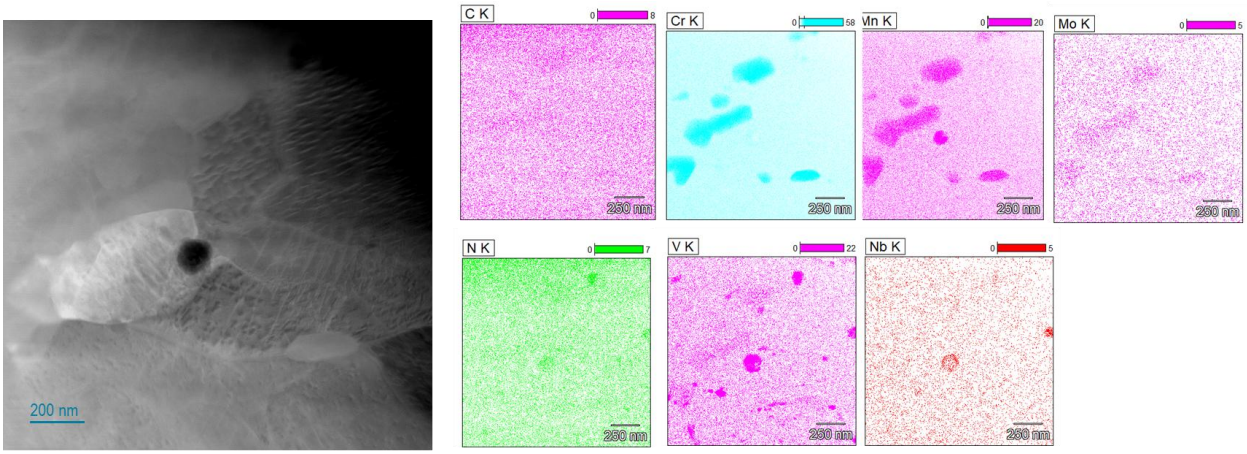

Figure 40. Microstructure and EDS analysis of G-92 steel after normalizing + tempering, indicating the presence of vanadium nitride at the lath boundaries.

6.2 Mechanical Properties

6.2.1 Vickers Hardness

Figure 41 presents the Vickers hardness measurements of DED G-92 steel across different heat treatment conditions, revealing systematic trends that directly correlate with the microstructural evolution and phase transformations occurring during thermal processing. The AD specimen exhibits an elevated hardness value of approximately 430 HV, attributed to the mixed F/M microstructure, high dislocation density, and residual stresses generated during the rapid solidification and thermal cycling inherent to the DED process. The normalized specimen demonstrates the highest hardness at approximately 460 HV, reflecting the formation of fresh, untempered martensite, which creates a hard but brittle microstructural state. The tempering treatment results in a significant hardness reduction to approximately 290 HV due to the tempering of martensite and the formation of a tempered martensitic structure with controlled carbide precipitation, which reduces brittleness while maintaining adequate strength levels. The two-step normalized plus tempered specimen exhibits the lowest hardness of approximately 250 HV, representing the optimal balance of strength and toughness achieved through the complete heat treatment cycle that produces tempered martensite with fine, uniformly distributed carbides. This systematic hardness progression validates the effectiveness of the thermal processing sequence in transforming the high-strength but potentially brittle AD and normalized conditions into the tougher, more ductile tempered martensitic microstructure required for nuclear reactor structural applications, where the combination of adequate strength and enhanced fracture toughness is essential for reliable long-term performance.

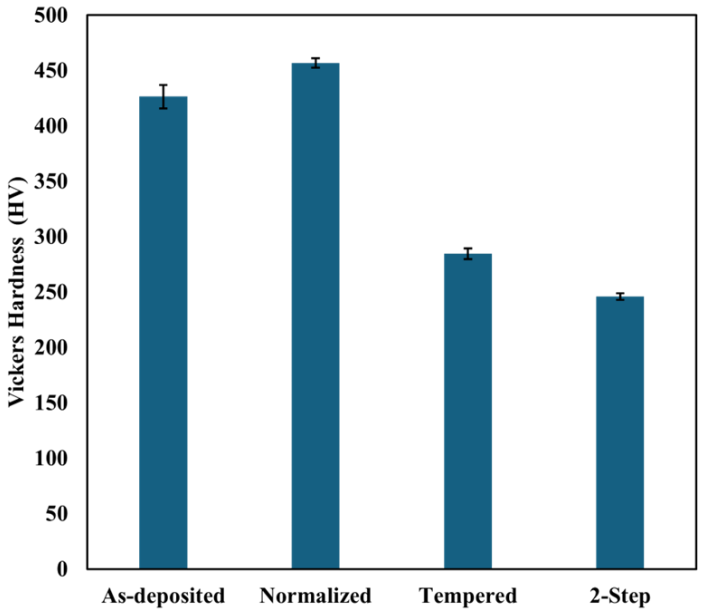

Figure 41. Vickers hardness of LP-DED Grade 92 steel before and after various heat treatments.

6.2.2 Uniaxial Tensile Testing

Figure 42 presents the RT engineering stress–strain behavior of DED G-92 steel in both the AD and tempered conditions, with specimens extracted in two orientations relative to the build direction. Figure 42 shows the complete stress–strain response, revealing significant processing-dependent mechanical behavior.

The AD specimens demonstrate exceptional strength levels with clear orientation-dependent characteristics. Horizontally extracted specimens [AD_Ha4 and AD_Hd1, red solid lines in Figure 42 achieve remarkable performance with a YS of approximately 1100–1200 MPa, a UTS reaching 1600–1700 MPa, and total elongations of 12%. These specimens exhibited classic ductile failure behavior with visible necking in the stress-strain curves, demonstrating substantial plastic deformation capacity before fracture.

Vertically extracted specimens [AD_Vd1 and AD_Va1, red dashed lines in Figure 42] show slightly reduced mechanical properties with a YS of approximately 1000 MPa, a UTS of 1570–1600 MPa and more limited elongations of 7.5%. Most significantly, these specimens displayed distinctly different fracture characteristics with abrupt failure behavior and no evidence of necking in the stress–strain curves, indicating orientation-dependent ductility limitations that suggest anisotropic microstructural features from the layered DED processing.

The stress–strain behavior of the specimens subjected to a tempering heat treatment effects are illustrated by the blue curves in Figure 42, showing a substantial strength reduction but improved ductility characteristics. Tempered horizontal specimens (Tempered_Ha1, blue solid line) achieve a YS of approximately850 MPa, a UTS of 1000 MPa, and elongations upto 12%. Tempered vertical specimens (Tempered_Vb1, blue dashed line) demonstrate similar mechanical properties with comparable strength levels.

Critical microstructural transformation effects are evident in the fracture behavior changes following tempering treatment. Both tempered horizontal and vertical specimens exhibited similar stress–strain characteristics with visible necking behavior and gradual load reduction, indicating that the tempering treatment successfully transformed the hard martensitic AD structure into tempered martensite and more uniform deformation characteristics across orientations. The room temperature tensile test data for G-92 steel is presented in Table 5.

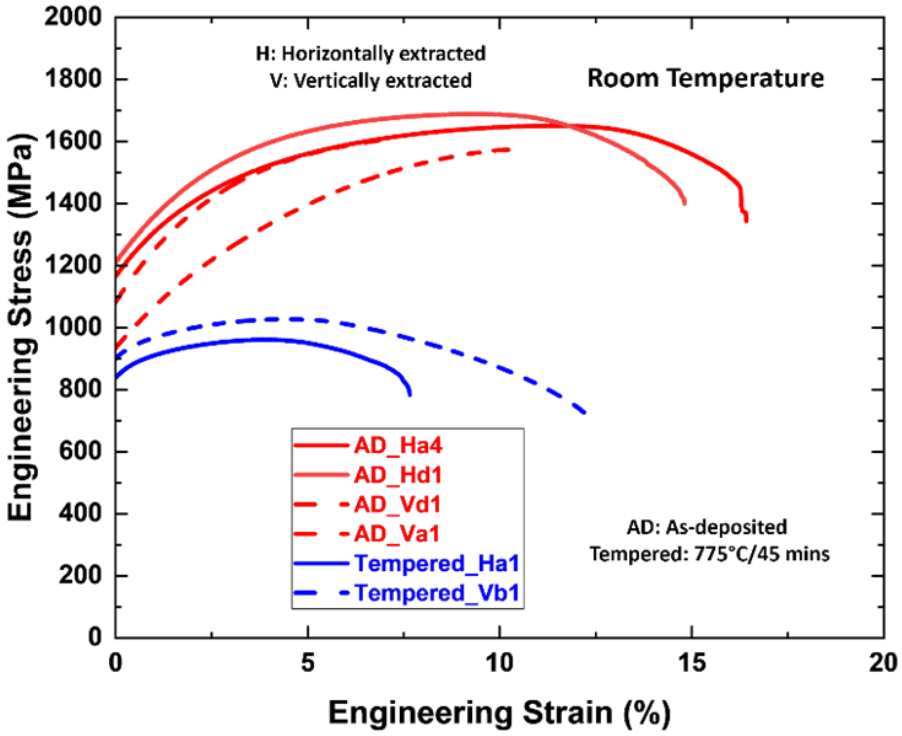

Figure 42. Engineering stress versus engineering strain plot of G-92 steel fabricated via LP-DED at RT.

Table 5. Room temperature tensile testing data of DED G-92 steel

Sample ID	Room Temperature		
	YS (MPa)	UTS (MPa)	El (%)
AD_Hd1	1208.84	1688.65	8.35
AD_Ha4	1165.14	1650.68	16.42
Avg. Horizontal	1187 ± 21.85	1669.67 ± 18.99	12.39 ± 4.04
AD_Va1	1082.78	1605.66	7.02
AD_Vd1	933.45	1573.18	7.97
Avg. Vertical	1008.12 ± 74.67	1589.42 ± 16.24	7.50 ± 0.48
Tempered_Ha1	837.98	961.12	7.66
Tempered_Vb1	899.42	1027.56	12.28

Figure 43 demonstrates the complex thermal–mechanical behavior of DED G-92 steel at reactor operating temperatures (550°C), revealing how elevated temperature exposure fundamentally alters the structure–property relationships established at RT. Figure 43 captures the temperature-activated deformation mechanisms through stress–strain analysis.

AD specimens achieve an approximate UTS of 1350 MPa regardless of extraction orientation (horizontal: AD_Hc1, AD_Hb4; vertical: AD_Vc2, AD_Va5), demonstrating that the martensitic microstructure develops potential thermal stability that promotes isotropic mechanical behavior under reactor conditions.

The blue curves exhibit clear separation between orientations, with vertical specimens (Tempered_Va3, blue dashed line) maintaining superior performance with a UTS of 715 MPa compared to that of the horizontal specimens [Tempered_Ha3, blue solid line in Figure 43] with a UTS of 654.

A comparison of the microstructural thermal sensitivity reveals fundamentally different temperature-dependent degradation mechanisms between processing conditions. The AD martensitic structure exhibits superior thermal stability with only a 15%–20% reduction in strength from that at RT. In contrast, the tempered microstructure shows enhanced thermal sensitivity with a 25%–30% reduction in strength.

The implications for reactor performance are that material selection must consider the complex interplay between the processing conditions, operating temperature, and component orientation, where AD G-92 steel provides more predictable thermal performance through reduced temperature-dependent anisotropy, while tempered conditions require careful orientation control and thermal management to maintain consistent mechanical properties during extended reactor service. The room temperature tensile test data for G-92 steel is presented in Table 6.

Table 6. Tensile testing data of DED G-92 steel at 550°C

Sample ID	550°C		
	YS (MPa)	UTS (MPa)	El (%)
AD_Hc1	1089.67	1413.88	6.47
AD_Hb4	1089	1272.58	5.24
Avg. Horizontal	1089.34 ± 0.34	1343.23 ± 70.65	5.86 ± 0.61
AD_Va5	1060.88	1363.13	5.55
AD_Vc2	1072.44	1354.73	5.09
Avg. Vertical	1066.66 ± 5.78	1358.93 ± 4.20	5.32 ± 0.23
Tempered_Ha3	613.68	654.28	7.82
Tempered_Va3	672.92	715.79	9.96

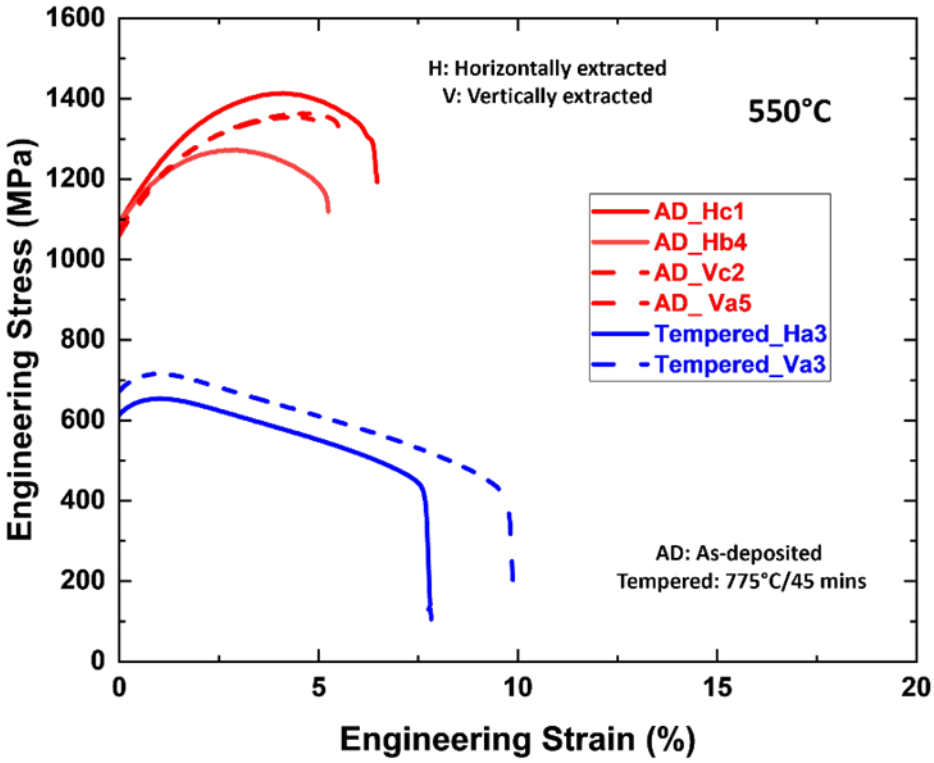

Figure 43. Engineering stress versus engineering strain plot of G-92 steel fabricated via DED at 550°C.

Figure 44 shows the temperature-dependent mechanical behavior of DED G-92 steel, revealing how the thermal exposure fundamentally alters the structure–property relationships between processing conditions and extraction orientation.

RT behavior: Figure 44(a) shows significant processing-dependent characteristics. AD specimens exhibit strong anisotropy with horizontal specimens (red solid lines) achieving a UTS of 1650–1700 MPa with necking behavior, while vertical specimens (red dashed lines) reach a UTS of ~1600 MPa but show abrupt fracture without necking. Tempered specimens demonstrate less anisotropy with both orientations (blue lines).

Elevated temperature behavior: Figure 44(b) reveals a complete anisotropy reversal. AD specimens now show remarkable isotropy with both orientations (red lines) converging to nearly identical performance, suggesting thermal activation eliminates orientation-dependent fracture mechanisms. Conversely, the tempered specimens develop significant anisotropy, with horizontal specimens (blue solid) maintaining a strength of ~650 MPa while vertical specimens (blue dashed) show improved performance at ~715 MPa.

Temperature effects demonstrate that the AD specimens retain ~85% of their RT strength at 550°C, while tempered specimens maintain only ~70%. This analysis provides critical insights for reactor component design, where material selection must consider the complex interactions between the processing conditions, operating temperature, and component orientation for nuclear applications.

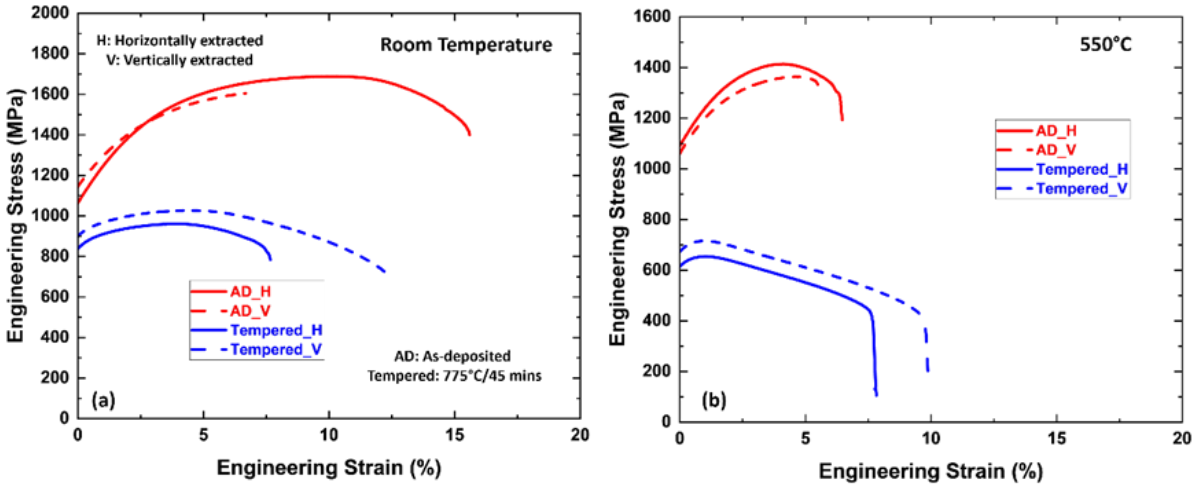

Figure 44. Representative engineering stress versus engineering strain plots of G-92 steel fabricated via LP-DED: (a) RT and (b) 550°C

Table 7 provides a comprehensive comparison of the YS values for F/M steels across different processing methods and alloy compositions, establishing the performance context of the current DED G-92 steel investigation within the broader literature.

Table 7. Reported YSs of F/M steels from the literature.

Alloys	Yield Strength, (MPa)	Ref.
LPBF G-91, as-deposited	~773	(Eftink et al. 2021)
DED G-91, as-deposited	~900	(Samuha et al. 2023)
WAAM G-91, as-deposited	-	(Robin et al. 2024)
WAAM G-91, as-deposited	~1026	(Sridharan and Field 2019)
Wrought G-91	~600	(Tong and Dai 2010)
DED G-92, as-deposited, per. to build direction	1338.48 ± 35.48	This study
DED G-92, as-deposited, par. to build direction	1258.25 ± 26.21	This study

6.3 Fractography

Figure 45 presents a low magnification fractographic analysis of AD G-92 steel specimens tested at RT and 550°C, revealing distinct temperature-dependent fracture characteristics and processing-related defects. The RT fractured specimen exhibited extensive crack propagation throughout the entire cross-sectional area, indicating widespread damage development during tensile loading that resulted in complex fracture path formation across the specimen gauge section.

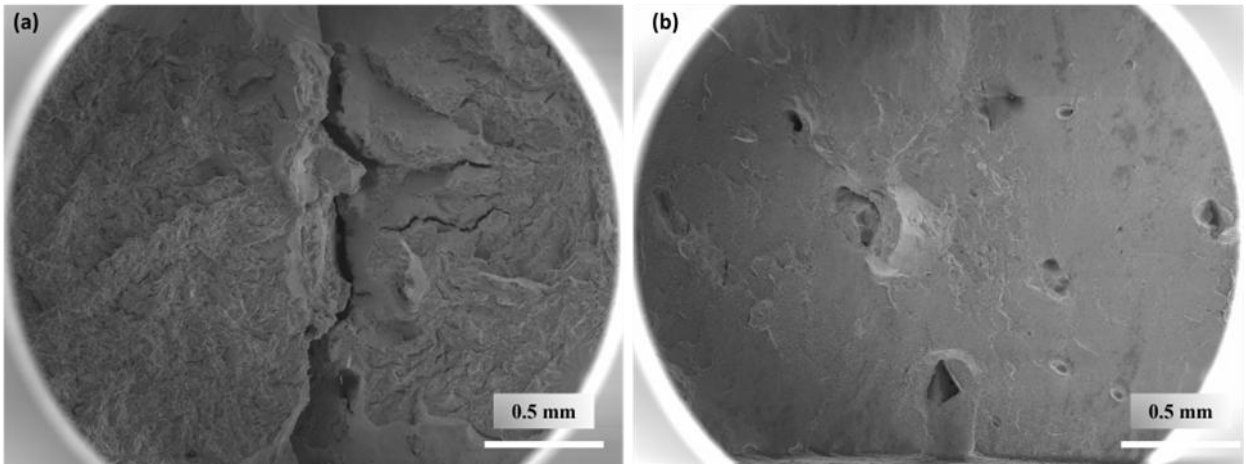

Figure 45. Fracture surface morphologies of AD G-92 steel tested at (a) RT and (b) 550°C.

In contrast, the elevated temperature (550°C) fractured specimen displayed the presence of large void-like pockets distributed across the fracture surface. A detailed examination revealed that these pockets ranged in size from 40–60 µm, as shown in Figure 45(b).

Both RT and elevated temperature specimens in Figures 45 and 46 exhibited a dimpled fracture morphology, which is characteristic of ductile failure mechanisms involving void nucleation, growth, and coalescence. The retention of ductile fracture behavior at both test temperatures demonstrates the inherent toughness of G-92 steel and indicates that the material maintains energy-absorbing failure mechanisms even in the presence of processing-induced defects. This ductile fracture characteristic is critical for nuclear structural applications where brittle failure must be avoided to ensure component reliability and safety during reactor operation.

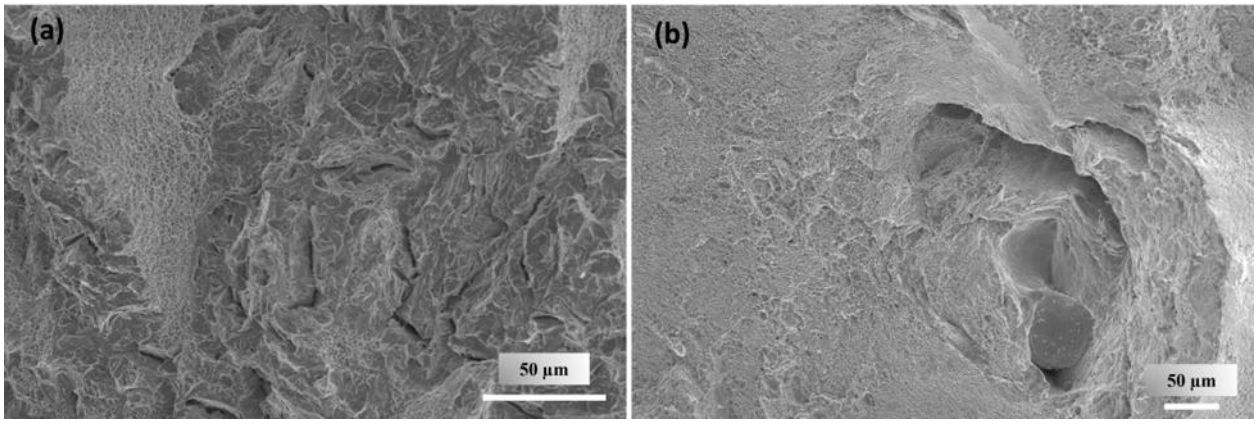

Figure 46. Representative fractured surface morphologies of AD G-92 steel tested at (a) RT and (b) 550 °C, taken at high magnification.

7.0 Summary

This investigation focused on establishing quantitative microstructure–property correlations in DED-manufactured A709 and G-92 steels by systematically analyzing how thermal processing modifications control microstructural development and influence mechanical performance across temperature ranges. The key findings and structure–property relationships for each steel are presented individually as follows:

DED A709:

- The exceptional mechanical properties of AD DED A709 steel (horizontal specimens: YS: 603 MPa, UTS: 844 MPa, 220 HV) arise from a complex multiscale strengthening architecture involving a fine cellular solidification structure with 2–3 μm cell walls within 10–50 μm grains, elevated dislocation densities from rapid thermal cycling during layer-by-layer deposition, grain boundary precipitates including NbC nodules distributed along chromium carbide phases, and residual stress states that collectively activate Hall–Petch grain boundary strengthening, dislocation strengthening, and precipitation hardening mechanisms to achieve 44% higher YS than that of the conventional wrought A709 material.
- Heat treatment modifications enable systematic microstructural control, where SA dissolves cellular boundaries and precipitates through diffusion-controlled homogenization to eliminate compositional gradients, PT retains the heterogeneous cellular morphology with preferential $M_{23}C_6$ carbide formation at cell walls, and the optimized SA+PT creates uniform dual precipitate populations consisting of $M_{23}C_6$ carbides at the grain boundaries and coherent MX Nb-rich carbonitrides (NbC/Nb(C, N)) distributed throughout the matrix.
- AD A709 steel shows persistent 12%–15% directional anisotropy with horizontal specimens achieving a higher strength (YS: 602 MPa) than that of the vertical specimens (YS: 529 MPa) due to the layered microstructure created during AM. This strength difference results from the DED process, which creates preferential grain orientations, aligned cellular boundaries, concentrated precipitates at cell walls, and directional dislocation patterns that make deformation easier in one direction than the other. Even after the combined SA+PT heat treatment, this anisotropy continues, with horizontal specimens maintaining a YS of 410 MPa compared to the YS of 371 MPa for vertical specimens, showing that the heat treatment cannot fully eliminate the directional microstructural features built into the material during the DED process.
- High-temperature testing at 550°C shows how the microstructure affects the performance under reactor operating conditions. The elevated temperature causes thermal softening through dislocation recovery, precipitate coarsening, and reduced strengthening mechanisms, leading to significant strength reductions of 40%–50% (AD horizontal specimen: decreases from 603 MPa to 437 MPa, SA+PT horizontal specimen: decreases from 410 MPa to 254 MPa). The high temperature also activates dynamic strain aging, where mobile atoms interact with dislocations during deformation, creating the characteristic serrated flow pattern seen in the stress–strain curves. Despite this thermal weakening, the refined DED microstructure still provides exceptional performance, maintaining 71% higher strength than that of the conventional wrought material (YS: 256 MPa) even at reactor operating temperatures, demonstrating the superior thermal stability of the additively manufactured microstructure.
- Fracture analysis establishes critical microstructure–toughness relationships, where the complex DED microstructure creates heterogeneous void nucleation behavior with both large processing-related pores from incomplete powder melting or gas entrapment and fine

microvoids that alter crack initiation and propagation compared to the uniform fine microvoid formation and intergranular failure mechanisms observed in wrought steel. Both processing conditions retain the essential ductile dimpled fracture morphology through microvoid nucleation, growth, and coalescence processes.

- Ion irradiation studies (100–400 dpa) demonstrate progressive radiation damage in AD DED A709 steel, with the maximum effects concentrated at a depth of 1 μm as predicted by SRIM calculations, where escalating dose levels reveal increasing void density and complex dislocation networks that contribute to radiation hardening and volumetric swelling. Further, persistent radiation-induced segregation creates intensifying Ni enrichment and Cr/Fe depletion that continue to evolve rather than saturating with extended exposure, which can ultimately compromise the corrosion resistance, local mechanical properties, and phase stability that are critical for the long-term integrity of nuclear reactor components in neutron irradiation environments.

DED G-92:

- The exceptional strength of AD DED G-92 steel (UTS, horizontal: 1650–1700 MPa, 430 HV) originates from a complex multiphase microstructure containing coexisting ferrite and martensite phases with incomplete martensitic transformation, an elevated GND density of $17.04\times10^{14}/m^2$ from rapid solidification thermal cycling, and fine needle-shaped θ-phase (Fe_3C) carbides distributed throughout the matrix. This combination of phase transformation strengthening, dislocation strengthening, and precipitation hardening mechanisms creates superior mechanical performance compared to that of conventional F/M steels.
- Heat treatment-induced microstructural modifications demonstrate distinct structure–property pathways, where normalizing alone produces the highest hardness (460 HV) through fresh untempered martensite formation with an increased GND density ($20.23\times10^{14}/m^2$). The tempering treatment develops the dual precipitation systems of $M_{23}C_6$ grain boundary carbides and MX-type (V, Nb)N nanoscale precipitates, but the hardness is reduced to 290 HV. Sequential normalizing–tempering achieves the optimal microstructural balance with the lowest hardness (250 HV) and a substantially reduced GND density ($11.01\times10^{14}/m^2$) through complete austenitization followed by controlled tempering-induced recovery and precipitation processes.
- The processing-dependent anisotropy reveals complex orientation–microstructure–property relationships. The AD specimens exhibit significant directional dependence, with horizontal specimens achieving a UTS of 1650–1700 MPa with ductile necking behavior while vertical specimens reach a UTS of ~1600 MPa but display abrupt brittle fracture without necking. This indicates that the layered DED microstructural architecture creates orientation-dependent fracture mechanisms. Tempering successfully reduces the RT anisotropy by transforming the hard martensitic AD structure into tempered martensite, enabling both horizontal and vertical specimens to exhibit similar stress–strain characteristics with visible necking behavior.
- The temperature-dependent behavior reveals a surprising anisotropy reversal. The AD specimens demonstrate superior high-temperature performance with only a 15%–20% reduction in strength at 550°C and complete elimination of the directional differences as both orientations achieve identical performance (UTS: ~1350 MPa). This suggests that the thermal energy activates deformation mechanisms that overcome the layered microstructural features. The tempered specimens show greater thermal sensitivity with a 25%–30% reduction in strength and the development of significant anisotropy at elevated

temperature (horizontal: 650–700 MPa versus vertical: 550–600 MPa), indicating that the tempered microstructure contains orientation-dependent thermal stability characteristics.

- A fracture mechanism analysis establishes the critical microstructure–toughness correlations where both the AD and tempered conditions maintain a ductile dimpled fracture morphology at room and elevated temperatures, confirming the retention of energy-absorbing failure mechanisms essential for nuclear applications. Results for elevated temperature exposure (550°C) reveal the formation of large void-like pockets (40–60 μm) distributed across the fracture surfaces that reflect the thermal activation of microstructural defects.

8.0 Future Scope of work

Further research on DED A709 and G-92 steels will establish fundamental structure–property relationships that govern temperature-dependent mechanical behavior from ambient to reactor operating conditions. This investigation will develop quantitative correlations between the microstructural architecture (grain structure, precipitate characteristics, dislocation networks, and defect populations) and critical mechanical properties (tensile strength, creep resistance, fracture toughness) to enable predictive material performance modeling and microstructural design optimization for nuclear applications.

Task 1: Temperature-Dependent Property Testing: Mechanical testing (tensile, creep, fracture toughness) will be conducted from RT to reactor conditions and directly correlated with a microstructural analysis. This will identify which structural features control deformation mechanisms at different temperatures and establish design criteria for nuclear qualification.

Task 2: Multiscale Microstructural Analysis: Advanced characterization (SEM/TEM, atom probe tomography) will quantify microstructural features at different length scales, including grain boundaries, precipitate distributions, dislocation networks, and chemical segregation. Statistical analyses will correlate these measured parameters with mechanical property variations to identify the most important structural factors controlling performance.

Task 3: Processing Optimization: Heat treatment protocols will be optimized using established structure–property relationships to achieve the target mechanical performance. Processing parameters will be adjusted to control precipitate characteristics, grain structure, and dislocation networks for maximum strength–ductility combinations. Validation testing will confirm that microstructural modifications produce predicted property improvements, demonstrating effective structure–property-driven optimization for nuclear applications.

9.0 Publications and Presentations

Journal Articles:

1. Subhashish Meher, Chinthaka M. Silva, Holden Hyer, Tanvi A. Ajantiwalay, Shalini Tripathi, Angel Ortiz, Quin R. S. Miller, Nathan Canfield, Mohan Sai Kiran Kumar Yadav Nartu, Sebastien Dryepondt, Isabella J. van Rooyen, Laser Powder Bed Fusion of ODS Fe–Cr–Al (0.3Zr, 0.3Y_2O_3): Unveiling Processing-Microstructure-Mechanical Property Relationships, planned for *Materials Science and Engineering A* (Submitted)
2. Asif Mahmud, Subhashish Meher, Peter Renner, Ariel Rieffer, Chinthaka Silva, John Snitzer, Qianwen Zhang, Xiaoyuan Lou, Isabella van Rooyen, Optimizing Directed Energy Deposition for G-91 and G-92 Ferritic/Martensitic Steels in Nuclear Environments: Linking Process Parameters to Microstructure, *Frontiers in Nuclear Engineering* (Submitted)
3. Subhashish Meher, Asif Mahmud, Chinthaka Silva, Peter Renner, Xiaoyuan Lou, John Snitzer, Qianwen Zhang, Lin Shao, Isabella van Rooyen, Process Optimization and Microstructural and Ion Irradiation Study of Directed Energy Deposition Fabricated A709, In preparation.
4. Subhashish Meher, Asif Mahmud, Isabella van Rooyen, Microstructural Control and Mechanical Property Optimization in Directed Energy Deposited A709 Austenitic Stainless Steel Through Heat Treatment Processing, *Materials Science and Engineering A*, In preparation.
5. Asif Mahmud, Subhashish Meher, Isabella van Rooyen, Post-Deposition Heat Treatment Effects on Phase Transformation and Tensile Behavior of DED G-92 Ferritic/Martensitic Steel, *Materials Science and Engineering A*, In preparation.

Conference Presentations:

1. Isabella van Rooyen, Subhashish Meher, Asif Mahmud, Srinivas Aditya Mantri, Xuan Zhang, Wei-Ying Chen, Evaluation of DED and LPBF Fe-Based Alloys Process Parameter Envelopes, *Structural Materials for Innovative Nuclear Systems (SMINS-7) 2025*, Spain.
2. Subhashish Meher, Asif Mahmud, German Valenzuela, Xiaoyuan Lou, John Snitzer, Isabella van Rooyen, Additive Manufacturing and Characterization of A709 Stainless Steels for Nuclear Applications, *TMS 2025*, Las Vegas, NV.
3. Subhashish Meher, Tianhao Wang, Mohan Nartu, David Garcia, Isabella van Rooyen, Advancing Nuclear Material Processing via Friction Stir Consolidation and Layer Deposition (Invited) *MS&T*, September 28–October 1, 2025, Columbus, Ohio.
4. Asif Mahmud, Subhashish Meher, Xiaoyuan Lou, John Snitzer, Isabella van Rooyen, Microstructure and Mechanical Properties of Heat-Treated Grade-92 Stainless Steels Fabricated by Directed Energy Deposition for Nuclear Applications, *MINES*, 2025, Cleveland, Ohio.

10.0 References

Alomari, A. S., N. Kumar, and K. L. Murty. 2018. “Enhanced Ductility in Dynamic Strain Aging Regime in a Fe-25Ni-20Cr Austenitic Stainless Steel.” *Materials Science and Engineering: A* 729: 157–160. https://doi.org/10.1016/j.msea.2018.05.060.

Bajaj, P., A. Hariharan, A. Kini, P. Kürnsteiner, D. Raabe, and E. A. Jägle. 2020. “Steels in Additive Manufacturing: A Review of Their Microstructure and Properties.” *Materials Science and Engineering: A* 772: 138633. https://doi.org/10.1016/j.msea.2019.138633.

Cui, L., S. Jiang, J. Xu, R. L. Peng, R. T. Mousavian, and J. Moverare. 2021. “Revealing Relationships between Microstructure and Hardening Nature of Additively Manufactured 316l Stainless Steel.” *Materials & Design* 198: 109385. https://doi.org/10.1016/j.matdes.2020.109385.

Ding, R., J. Yan, H. Li, S. Yu, A. Rabiei, and P. Bowen. 2019. “Deformation Microstructure and Tensile Properties of Alloy 709 at Different Temperatures.” *Materials & Design* 176: 107843. https://doi.org/10.1016/j.matdes.2019.107843.

Eftink, B. P., D. A. Vega, O. El Atwani, D. J. Sprouster, Y. S. J. Yoo, T. E. Steckley, E. Aydogan, C. M. Cady, M. Al-Sheikhly, T. J. Lienert, and S. A. Maloy. 2021. “Tensile Properties and Microstructure of Additively Manufactured Grade 91 Steel for Nuclear Applications.” *Journal of Nuclear Materials* 544: 152723. https://doi.org/10.1016/j.jnucmat.2020.152723.

El-Atwani, O., B. P. Eftink, C. M. Cady, D. R. Coughlin, M. M. Schneider, and S. A. Maloy. 2021. “Enhanced Mechanical Properties of Additive Manufactured Grade 91 Steel.” *Scripta Materialia* 199: 113888. https://doi.org/10.1016/j.scriptamat.2021.113888.

Kim, H., J. G. Gigax, J. Fan, F. A. Garner, T.-L. Sham, and L. Shao. 2019. “Swelling Resistance of Advanced Austenitic Alloy 709 and Its Comparison with 316 Stainless Steel at High Damage Levels.” *Journal of Nuclear Materials* 527: 151818. https://doi.org/10.1016/j.jnucmat.2019.151818.

Klueh, R. L., and A. T. Nelson. 2007. “Ferritic/Martensitic Steels for Next-Generation Reactors.” *Journal of Nuclear Materials* 371 (1): 37–52. https://doi.org/10.1016/j.jnucmat.2007.05.005.

Konijnenberg, P. J., S. Zaefferer, and D. Raabe. 2015. “Assessment of Geometrically Necessary Dislocation Levels Derived by 3D EBSD.” *Acta Materialia* 99: 402–414. https://doi.org/10.1016/j.actamat.2015.06.051.

Li, M., Z. Zeng, Y. Momozaki, D. L. Rink, and J. Listwan. 2021. *Progress Report on Performance of A709 and G91 Steels in Sodium.* Argonne National Laboratory ANL-ART-232. Argonne, IL. https://www.osti.gov/biblio/1818065.

Liu, X. 2018. “Radiation-Induced Microstructural and Mechanical Property Modifications in Advanced Alloys.” PhD dissertation, University of Illinois at Urbana-Champaign.

Mantri, S. A., X. Zhang, and W. Y. Chen. 2025. “Influence of Post Deposition Annealing on the Microstructural Evolution and Tensile Behavior of Austenitic Stainless-Steel Alloy 709 Made by Laser Powder Bed Fusion.” *Materials Science and Engineering: A* 927: 148054. https://doi.org/10.1016/j.msea.2025.148054.

Moussa, C., M. Bernacki, R. Besnard, and N. Bozzolo. 2015. “About Quantitative EBSD Analysis of Deformation and Recovery Substructures in Pure Tantalum.” *IOP Conference Series: Materials Science and Engineering* 89: 012038. https://doi.org/10.1088/1757-899x/89/1/012038.

Pantleon, W. 2008. “Resolving the Geometrically Necessary Dislocation Content by Conventional Electron Backscattering Diffraction.” *Scripta Materialia* 58 (11): 994–997. https://doi.org/10.1016/j.scriptamat.2008.01.050.

Robin, I. K., D. J. Sprouster, N. Sridharan, L. L. Snead, and S. J. Zinkle. 2024. “Synchrotron Based Investigation of Anisotropy and Microstructure of Wire Arc Additive Manufactured Grade 91 Steel.” *Journal of Materials Research and Technology* 29: 5010–5021. https://doi.org/10.1016/j.jmrt.2024.02.230.

Samuha, S., J. Bickel, T. Mukherjee, T. DebRoy, T. J. Lienert, S. A. Maloy, C. R. Lear, and P. Hosemann. 2023. “Mechanical Performance and Microstructure of the Grade 91 Stainless Steel Produced Via Directed Energy Deposition Laser Technique.” *Materials & Design* 227: 111804. https://doi.org/10.1016/j.matdes.2023.111804.

Sham, T.-L., R. E. Bass, Y. Wang, and X. Zhang. 2022. *A709 Qualification Plan Update and Mechanical Properties Data Assessment.* Idaho National Laboratory INL/RPT-22-67641-Rev000. Idaho Falls, ID. https://www.osti.gov/biblio/1906516.

Shrestha, T., S. F. Alsagabi, I. Charit, G. P. Potirniche, and M. V. Glazoff. 2015. “Effect of Heat Treatment on Microstructure and Hardness of Grade 91 Steel.” *Metals* 5 (1): 131–149. https://www.mdpi.com/2075-4701/5/1/131.

Sridharan, N., and K. Field. 2019. “A Road Map for the Advanced Manufacturing of Ferritic-Martensitic Steels.” *Fusion Science and Technology* 75 (4): 264–274. https://doi.org/10.1080/15361055.2019.1577124.

Tong, Z., and Y. Dai. 2010. “The Microstructure and Tensile Properties of Ferritic/Martensitic Steels T91, Eurofer-97 and F82H Irradiated up to 20dpa in STIP-III.” *Journal of Nuclear Materials* 398 (1-3): 43–48. https://doi.org/10.1016/j.jnucmat.2009.10.008.

Wang, Y., P. Hou, R. E. Bass, X. Zhang, and T. L. Sham. 2022. *Interim Mechanical Properties Data from FY2022 ORNL Testing of A709 with Precipitation Treatment for ASME Code Case Data Package.* Oak Ridge National Laboratory ORNL/TM-2022/2593. Oak Ridge, TN. https://www.osti.gov/biblio/1887676.

Wanni, J., J. G. Michopoulos, and A. Achuthan. 2022. “Influence of Cellular Subgrain Feature on Mechanical Deformation and Properties of Directed Energy Deposited Stainless Steel 316 l.” *Additive Manufacturing* 51: 102603. https://doi.org/10.1016/j.addma.2022.102603.

Zhang, X., W.-Y. Chen, and A. Caputo. 2021. “In-Situ Ion Irradiation Study of Alloy 709 Stainless Steels with Different Processing Histories.” *Journal of Nuclear Materials* 553: 153052. https://doi.org/10.1016/j.jnucmat.2021.153052.

Zhao, Y., M. N. Cinbiz, J.-S. Park, J. Almer, and D. Kaoumi. 2020. “Tensile Behavior and Microstructural Evolution of a Fe-25Ni-20Cr Austenitic Stainless Steel (Alloy 709) from Room to Elevated Temperatures through in-Situ Synchrotron X-Ray Diffraction Characterization and Transmission Electron Microscopy.” *Journal of Nuclear Materials* 540: 152367. https://doi.org/10.1016/j.jnucmat.2020.152367.

Pacific Northwest National Laboratory

902 Battelle Boulevard
P.O. Box 999
Richland, WA 99354

1-888-375-PNNL (7665)

www.pnnl.gov